nature chemical biology

Article

https://doi.org/10.1038/s41589-024-01803-1

Chemically engineered antibodies for autophagy-based receptor degradation

Received: 9 July 2023

Accepted: 19 November 2024

Binghua Cheng[1,2,3,6], Meiqing Li[1,4,6], Jiwei Zheng[1,3,6], Jiaming Liang[1,2,3], Yanyan Li[1,2,3], Ruijing Liang[1,3,4], Hui Tian[1,5], Zeyu Zhou[1,5], Li Ding[1], Jian Ren[1,2], Wenli Shi[1], Wenjie Zhou[1,5], Hailiang Hu[5], Long Meng[1,3], Ke Liu[1,4], Lintao Cai[1,3,4] ✉, Ximing Shao[1,4] ✉, Lijing Fang[1,3,4] ✉ & Hongchang Li[1,3,4] ✉

Cell surface receptor-targeted protein degraders hold promise for drug discovery. However, their application is restricted because of the complexity of creating bifunctional degraders and the reliance on specific lysosome-shuttling receptors or E3 ubiquitin ligases. To address these limitations, we developed an autophagy-based plasma membrane protein degradation platform, which we term AUTABs (autophagy-inducing antibodies). Through covalent conjugation with polyethylenimine (PEI), the engineered antibodies acquire the capacity to degrade target receptors through autophagy. The degradation activities of AUTABs are self-sufficient, without necessitating the participation of lysosome-shuttling receptors or E3 ubiquitin ligases. The broad applicability of this platform was then illustrated by targeting various clinically important receptors. Notably, combining specific primary antibodies with a PEI-tagged secondary nanobody also demonstrated effective degradation of target receptors. Thus, our study outlines a strategy for directing plasma membrane proteins for autophagic degradation, which possesses desirable attributes such as ease of generation, independence from cell type and broad applicability.

Cell surface signaling receptors represent important therapeutic targets for the treatment of diverse human diseases, including cancer and autoimmune disorders[1,2]. Therefore, the development of efficacious strategies to selectively inhibit the function of this class of proteins has a potential to improve human health[3,4]. In comparison to conventional inhibition-based therapeutics, the novel concept of targeted protein degradation provides a more powerful approach to eliminate the surface target of interest[5]. While classical targeted protein degraders, such as proteolysis-targeting chimeras (PROTACs), have demonstrated remarkable efficacy in targeting traditionally challenging proteins, their applicability is limited to cytosolic proteins because of the exclusive presence of their targeted degradation machinery, proteasomes, in the cytoplasm[6]. To broaden the range of targeted protein degradation to encompass plasma membrane proteins, a number of intelligent technologies have been recently developed that include lysosome-targeting chimeras, molecular degraders of extracellular proteins through the asialoglycoprotein receptor, antibody-based PROTACs, proteolysis-targeting antibodies and cytokine receptor-targeting chimeras[7–12]. Despite variations in individual design strategies, the fundamental mechanism of action for these degraders is designed to tether the targeted membrane protein to either membrane-associated E3 ubiquitin ligases[10,11] or membrane-bound lysosome-shuttling

---

[1] Guangdong Key Laboratory of Nanomedicine, CAS-HK Joint Lab of Biomaterials, Shenzhen Institute of Advanced Technology, Chinese Academy of Sciences, Shenzhen, China. [2] University of Chinese Academy of Sciences, Beijing, China. [3] Key Laboratory of Biomedical Imaging Science and System, Chinese Academy of Sciences, Shenzhen, China. [4] Sino-Euro Center of Biomedicine and Health, Shenzhen, China. [5] Department of Biochemistry, School of Medicine, Southern University of Science and Technology, Shenzhen, China. [6] These authors contributed equally: Binghua Cheng, Meiqing Li, Jiwei Zheng. ✉e-mail: lt.cai@siat.ac.cn; xm.shao@siat.ac.cn; lj.fang@siat.ac.cn; hc.li@siat.ac.cn

receptors[7–9,12], resulting in hijacked ubiquitination or internalization of the target protein for lysosome degradation. As such, the development of these technologies necessitates the complex generation of bifunctional degraders capable of simultaneously binding to two targets with high affinity and correct conformation. Additionally, the expression of targeted E3 ubiquitin ligases and membrane receptors varies substantially across different cell types and tissues, thereby restricting the clinical utility of these technologies. Thus, there is still an urgent need to devise a more streamlined approach for degradation of cell surface receptors.

The ubiquitin–proteasome system (UPS) and autophagy are the two major intracellular degradation mechanisms[13]. Inspired by the successful development of PROTACs that selectively degrade proteins through hijacking UPS machinery, technologies with the aim of repurposing autophagy to degrade certain target proteins are recently attracting attention. The representative degraders that fall into this class are autophagy-targeting chimeras (AUTACs/AUTOTACs) and autophagy-tethering compounds (ATTECs)[14–16]. Autophagy-targeting degraders may offer advantages over UPS-based degraders, particularly when the destruction of large components such as protein aggregates and intracellular organelles is required. Indeed, AUTACs have been successfully used to degrade damaged mitochondria[14], while ATTECs and AUTOTACs have shown promise to eliminate pathologic protein aggregates in neurons[15,16]. However, these autophagy-targeting degraders are all restricted to cytosolic proteins or organelles. Given that cell surface receptors typically exhibit substantial molecular masses and usually form homozygous or heterozygous complexes, harnessing the power of autophagy to degrade these large molecules presents a promising avenue for investigation. In this study, we explore this possibility by generating engineered antibodies that are conjugated with autophagy-inducing chemicals. We envision that these autophagy-inducing antibodies (AUTABs) will activate the intrinsic autophagy machinery upon binding to their targeted receptors, eventually leading to the degradation of these plasma-membrane-associated proteins through the autophagic–lysosomal pathway.

Results

Autophagy induction upon polyethylenimine treatment

Polyethylenimine (PEI) is popular for gene transfer because of its excellent transmembrane delivery. Studies have suggested that it also induces autophagy[17,18]. Thus, we chose PEI as the autophagy-inducing agent for our AUTAB platform establishment, hypothesizing that linking an antibody to PEI would promote internalization and lysosomal degradation of its target receptor through autophagy. To test this hypothesis, we initially investigated PEI's impact on autophagy induction. Using 25-kDa linear PEI (L25K PEI), we found a significant dose-dependent and time-dependent increase in LC3B-II proteins, indicating autophagy activation (Fig. 1a,b). Additionally, fluorescein isothiocyanate (FITC)-labeled PEI showed minimal overlap with LC3B puncta but more overlap with another ATG8 family protein, LC3C (Fig. 1c,d and Extended Data Fig. 1a).The phenomenon was not because of the FITC label, as neither FITC nor FITC-conjugated transferrin induced autophagy (Supplementary Fig. 1). PEI treatment caused LC3C puncta to accumulate within 1 h, whereas LC3B puncta appeared only after 6 h (Extended Data Fig. 1b,c). These results suggest that PEI treatment prefers to trigger LC3C-mediated autophagy, an unconventional pathway crucial for eliminating endocytosed plasma membrane cargos[19]. Consistent with this discovery, the PEI-induced LC3C-positive autophagosomes colocalized with early (Rab5) and late (Rab7) endosome markers (Fig. 1e,f and Extended Data Fig. 1a). Furthermore, these autophagosomes followed the typical autophagy pathway, ending up in lysosomes marked with red fluorescent protein (RFP)–Lamp1 for degradation (Fig. 1g and Extended Data Fig. 1a). Collectively, these data demonstrated that PEI triggers autophagy through an LC3C-dependent pathway after entering endosomes.

Previous research has shown a strong link between membrane damage and LC3C-mediated autophagy[20–22]. Because PEI, a cationic polymer, can bind to negatively charged lipids in membranes, it likely damages the endosomal membrane, potentially triggering autophagy. Using galectin 3, a sensor for membrane damage, we observed clear endosomal membrane damage in PEI–FITC-treated cells (Fig. 1h and Extended Data Fig. 1a). Therefore, we conclude that PEI likely induces autophagy by introducing endosomal membrane damage.

We also investigated whether this property is consistent across various PEI types. As shown, both linear and branched PEIs, ranging from 800 to 25,000 Da, induced a similar level of LC3C-mediated autophagy, indicating that PEI triggers autophagy regardless of molecular size and structure. (Fig. 1i,j and Extended Data Fig. 1a).

Together, our results reveal a mechanism by which PEI induces autophagy. Upon cellular internalization by endocytosis, PEI induces damage on the endosomal membrane, consequently leading to activation of the LC3C-mediated autophagy pathway and subsequent redirection of endosomes toward lysosomal degradation (Fig. 1k).

Development of the AUTAB degrader targeting programmed cell death ligand 1

Next, we hypothesized that conjugation of PEI to an antibody would facilitate endocytosis and further direction of its targeting receptor for lysosomal degradation by triggering autophagic machinery (Fig. 2a). As a proof-of-principle experiment, we synthesized an AUTAB molecule (Atz-AUTAB) to target the immunotherapy target programmed cell death ligand 1 (PDL1) by covalent conjugating PEI to atezolizumab (Atz), an anti-PDL1 antibody drug approved by the Food and Drug Administration (FDA) for cancer therapy. To create Atz-AUTAB, lysine residues on the Atz antibody were nonspecifically functionalized with succinimidyl 6-azidohexanoate (N_3-C5-NHS) and Atz-N_3 formation was monitored by agarose gel electrophoresis (Supplementary Fig. 2a,b). Matrix-assisted laser desorption/ionization time-of-flight mass spectrometry (MALDI-TOF MS) analysis showed an average of 10.3 azide ligands per antibody (Supplementary Fig. 2c). The Atz was then covalently linked to PEI through copper-free strain-promoted azide–alkyne cycloaddition (SPAAC) between Atz-N_3 and dibenzocyclooctyne (DBCO)-labeled PEI, which was produced by reacting L25K PEI with DBCO-NHS (Fig. 2b and Supplementary Fig. 2a). The resulted Atz-AUTAB was confirmed by denaturing gel electrophoresis in which the PEI-conjugated antibodies showed expected slower migration than nonmodified ones (Fig. 2c).

We first examined the effect of Atz-AUTAB in HeLa cells stably expressing HA–PDL1. As shown, although Atz treatment induced a certain degree of PDL1 endocytosis, the vesicles lacked galectin 3, indicating no endosomal membrane damage. Conversely, Atz-AUTAB led to notable PDL1 endocytosis and endosomal membrane damage, shown by galectin 3 accumulation on the vesicles (Fig. 2d and Extended Data Fig. 2a). Thereafter, Atz-AUTAB further activated autophagy by recruiting LC3C proteins on damaged endosomes (Fig. 2e and Extended Data Fig. 2a). This outcome was confirmed using GFP–RFP–LC3 cell lines, where Atz-AUTAB notably stimulated LC3C but not LC3B autophagic flux (Supplementary Fig. 3a,b). Consistent with these results, the internalized PDL1 receptors were observed to traffic to lysosomes in cells exposed to Atz-AUTAB (Fig. 2f and Extended Data Fig. 2a). In contrast, in cells treated with Atz alone, most endosomes containing PDL1 dispersed in the cytoplasm, with only a small portion reaching lysosomes, indicating a dominant nonlysosome toward trafficking of PDL1 in these cells (Fig. 2f and Extended Data Fig. 2a). Notably, endosomal PDL1 and Atz-AUTAB consistently colocalized, indicating that they were endocytosed as a complex. Collectively, our data suggest that AUTAB degraders can redirect targeted receptors to lysosomes for degradation by activating the autophagic pathway.

In contrast to PEI, Atz-AUTAB exclusively generated LC3C-positive autophagosomes, with no presence of LC3B (Supplementary Fig. 3c,d).

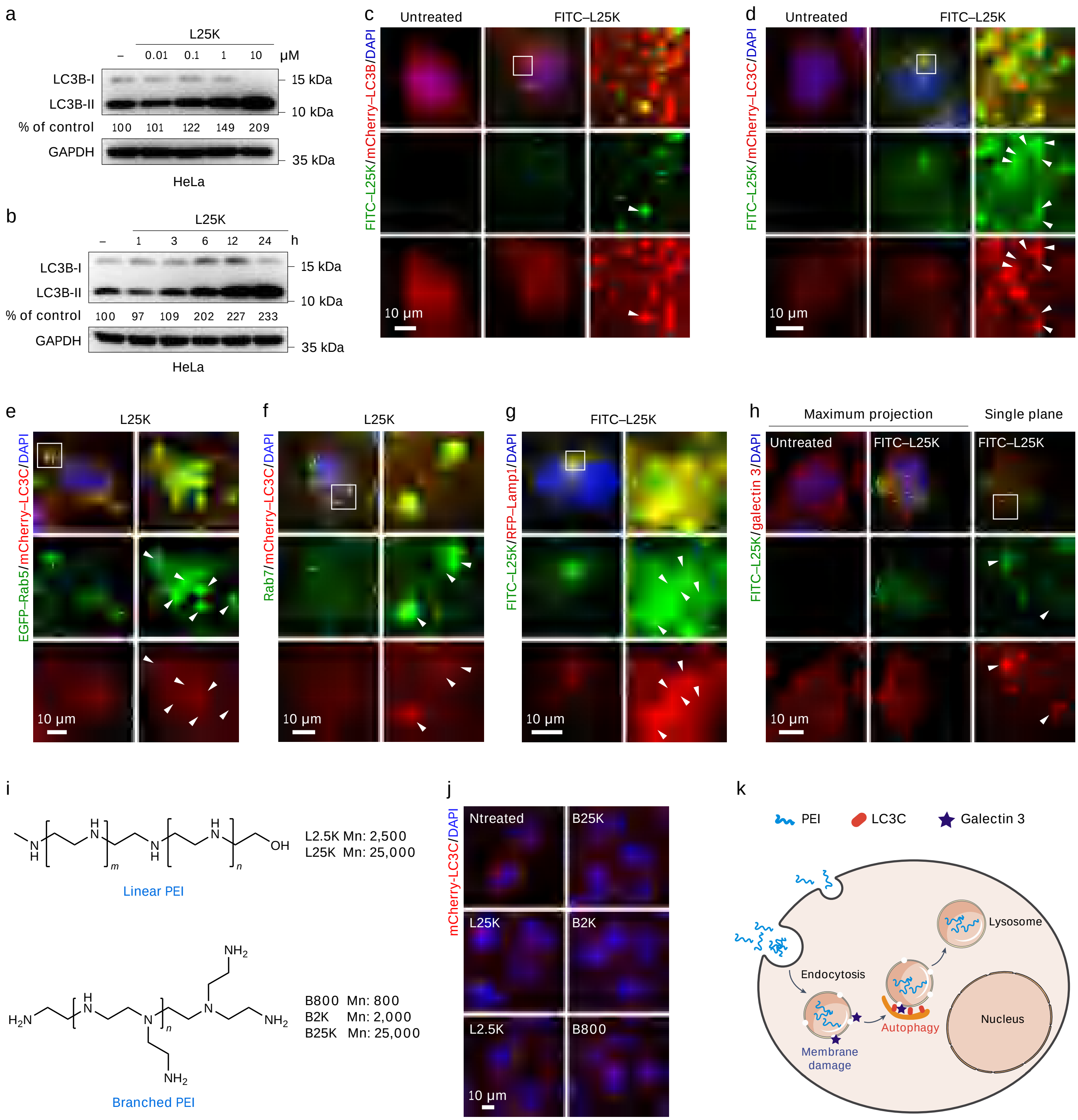

Fig. 1 | PEI induces LC3C-dependent autophagy. a,**b**, Western blot analysis of the autophagy marker protein LC3B in HeLa cells treated with increasing concentrations of L25K PEI for 4 h (**a**) or 0.1 μM L25K PEI for the indicated times (**b**). **c**,**d**, Representative confocal images of HeLa cells stably expressing mCherry–LC3B (**c**) or mCherry–LC3C (**d**) treated with or without 10 μM FITC-labeled L25K PEI for 3 h. Right: enlarged views of the white boxed regions. The arrowheads indicate the colocalization between FITC–L25K PEI and mCherry–LC3B (**c**) or mCherry–C3C (**d**). **e**,**f**, Representative confocal images showing the colocalization of LC3C with Rab5-positive (**e**) or Rab7-positive (**f**) endosomes in mCherry–LC3C stably expressing HeLa cells upon treatment with 10 μM L25K PEI for 1 h. Cells were transiently transfected with EGFP–Rab5 1 day before treatment (**e**) or stained for endogenous Rab7 after treatment (**f**). Right: enlarged views of the white boxed regions. The arrowheads point to the colocalization of mCherry–LC3C with EGFP–Rab5 or Rab7. **g**, HeLa cells transiently expressing RFP–Lamp1 were treated with 10 μM FITC–L25K PEI for 6 h, fixed and imaged by confocal microscopy. Right: enlarged view of the white boxed region. The colocalization of FITC–L25K with RFP–Lamp1 is indicated by white arrowheads. **h**, HeLa cells were treated with or without 10 μM FITC–L25K PEI for 1 h, fixed and stained for galectin 3. *Z*-stack confocal images of cells were taken and are presented as maximum projections or single planes. Bottom: enlarged views of the white boxed regions, in which the colocalization of FITC–L25K with galectin 3 is indicated by white arrowheads. **i**, Structure illustration of linear and branched PEI with various molecular weights. **j**, Representative images of mCherry–LC3C stably expressing HeLa cells upon treatment with 25 μg ml^{-1} of various types of PEI (L25K, L2.5K, B25K, B2K and B800) for 1 h. **k**, Schematic to illustrate the LC3C-dependent autophagy induced by PEI treatment. DNA in **c**–**h**,**j** was counterstained with DAPI. Scale bars, 10 μm.

https://doi.org/10.1038/s41589-024-01803-1

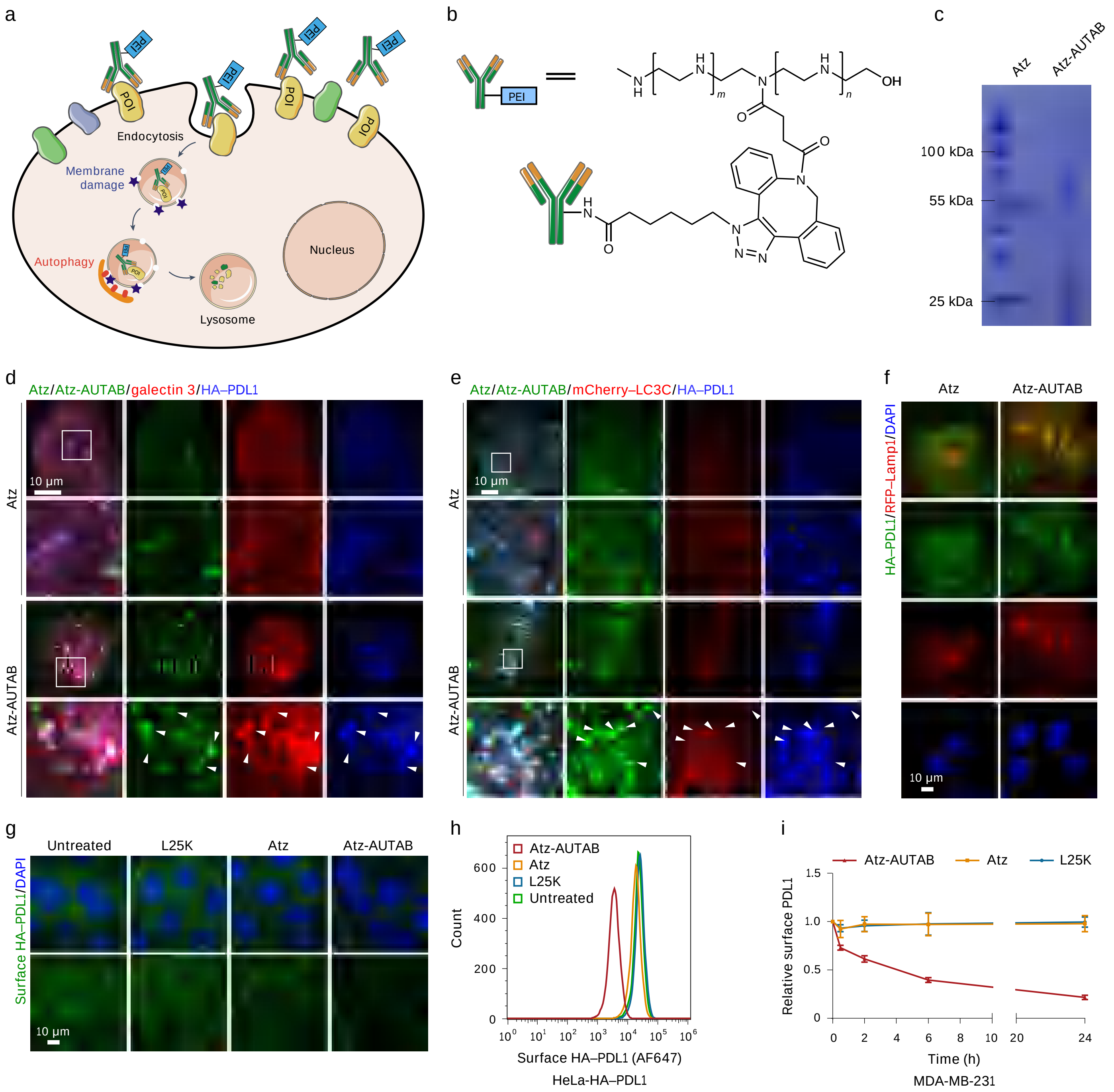

Fig. 2 | Development of Atz-AUTAB to target PDL1. a, Schematic of the AUTAB platform designed for targeting degradation of cell surface receptors. **b**, Structure of the Atz-AUTABs that were prepared by covalent conjugation of L25K PEI with atezolizumab through SPAAC. **c**, SDS–PAGE analysis of the Atz-AUTABs with Coomassie blue staining. **d**, HeLa cells stably expressing HA–PDL1 were treated with 100 nM Atz or Atz-AUTAB for 1 h. Cells were then fixed, costained using antibodies to Atz, galectin 3 and HA and imaged by confocal microscopy. Bottom: enlarged views of the boxed regions. The arrowheads point to the colocalization of Atz-AUTAB, galectin 3 and HA–PDL1. **e**, HeLa cells stably expressing HA–PDL1 and mCherry–LC3C were treated with Atz or Atz-AUTAB as in **d**. Cells were then fixed, costained with antibodies to Atz and HA and imaged. Bottom: enlarged views of the boxed regions. The arrowheads indicate the triple colocalization of Atz-AUTAB, mCherry–LC3C and HA–PDL1. **f**, Representative confocal images showing the colocalization of HA–PDL1 with RFP–Lamp1 in HeLa cells stably expressing HA–PDL1 upon 1 h of treatment with 5 nM Atz or Atz-AUTAB. Cells were transiently transfected with RFP–Lamp1 1 day before the treatment. **g**, HeLa cells stably expressing HA–PDL1 were treated with 10 nM L25K PEI, 5 nM Atz or 5 nM Atz-AUTAB for 4 h. Cells were then fixed, stained for surface HA–PDL1 and imaged by confocal microscopy. **h**, Live-cell flow cytometry showing the levels of cell-surface PDL1 in HeLa cells expressing HA–PDL1 following treatment as in **g**. **i**, Flow cytometry analysis of surface PDL1 levels in live MDA-MB-231 cells incubated with 10 nM L25K PEI, 5 nM Atz or 5 nM Atz-AUTAB for different periods of time (0.5, 2, 6 and 24 h). Mean fluorescence intensity of surface PDL1 relative to the untreated group was quantified (*n* = 3 biological replicates, means ± s.d.). DNA in **f**,**g** was counterstained with DAPI. Scale bars, 10 μm.

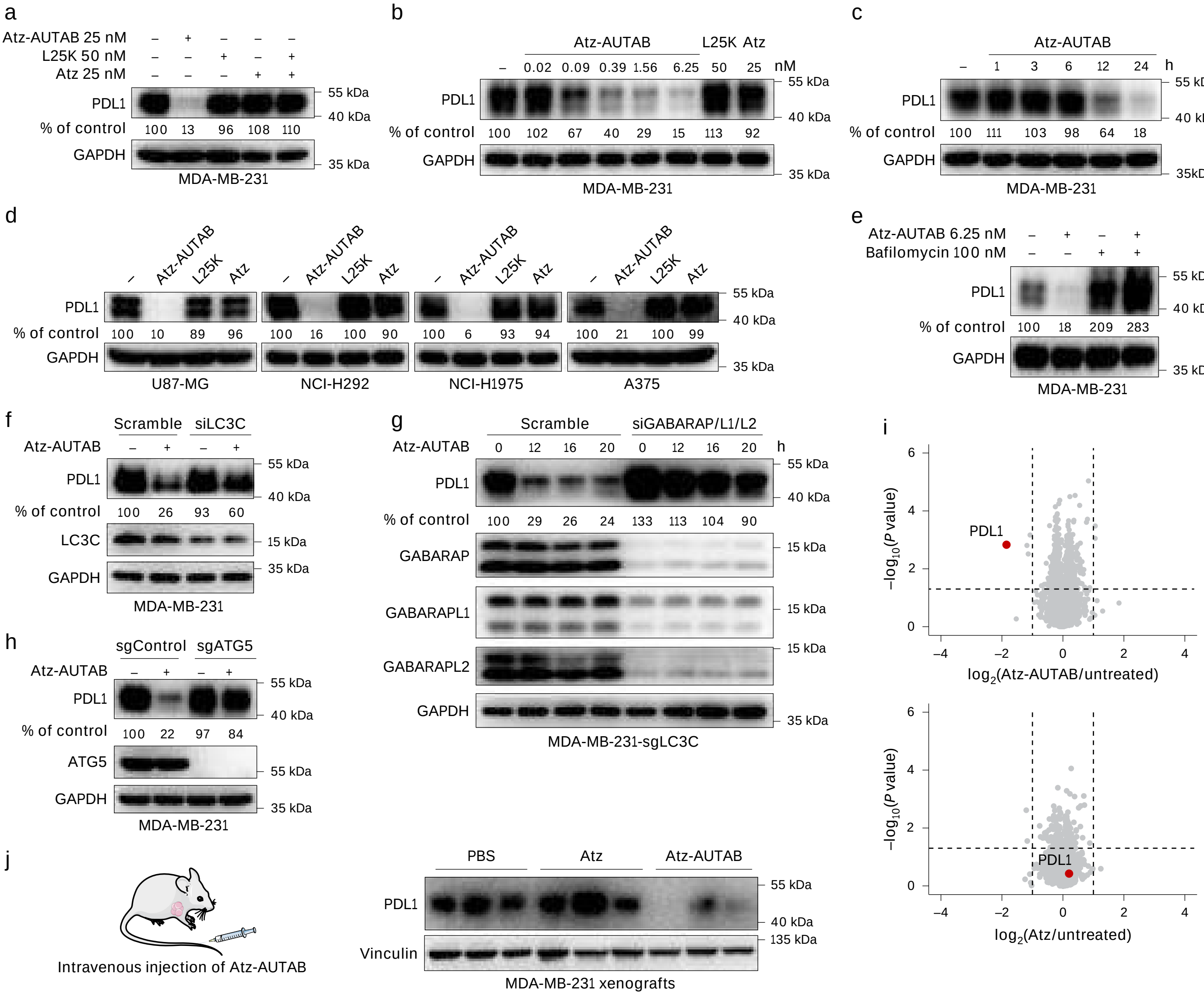

Fig. 3 | Atz-AUTAB drives PDL1 degradation through autophagic–lysosomal pathway. a, Western blot analysis of the endogenous PDL1 levels in MDA-MB-231 cells treated with L25K PEI, Atz, an Atz–L25K PEI mixture or Atz-AUTAB for 24 h at the indicated concentrations. **b**, Western blotting to detect the dose response of PDL1 degradation in MDA-MB-231 cells incubated with increasing concentrations of Atz-AUTAB for 24 h. **c**, Western blot analysis of PDL1 in MDA-MB-231 cells treated with 6.25 nM Atz-AUTAB for the indicated times. **d**, The levels of PDL1 in U87-MG, NCI-H292, NCI-H1975 and A375 cells upon treatment with 50 nM L25K PEI, 25 nM Atz or 25 nM Atz-AUTAB for 24 h. **e**, Western blot analysis of the PDL1 degradation in MDA-MB-231 cells treated with Atz-AUTAB for 24 h in the presence or absence of bafilomycin A1 at the indicated concentrations. **f**, Western blot of PDL1 in MDA-MB-231 cells treated with 6.25 nM Atz-AUTAB for 12 h under siRNA-mediated knockdown of *LC3C*. **g**, Western blot of PDL1 in *LC3C*-knockout MDA-MB-231 cells treated with 6.25 nM Atz-AUTAB for the indicated time (0, 12, 16 or 20 h) under siRNA-mediated codeletion of *GABARAP*, *GABARAPL1* and *GABARAPL2*. **h**, Western blot of PDL1 in *ATG5*-knockout MDA-MB-231 cells treated with 6.25 nM Atz-AUTAB for 12 h. **i**, Quantitative proteomic analysis of MDA-MB-231 cells treated with 25 nM Atz-AUTAB or Atz for 24 h. Volcano plots display the fold change in the average abundance of 6,616 proteins from three independent experiments. PDL1 is indicated by the red dot. **j**, Western blot of PDL1 in MDA-MB-231 xenografts after intravenous administration of 5 mg kg^{-1} Atz or Atz-AUTAB once daily for 3 days ($n = 3$ mice per group). Statistical significance was calculated using an unpaired two-tailed Student's *t*-test (**i**).

Additionally, Atz-AUTAB-induced autophagy relies on PDL1 endocytosis. Knockdown of *PDL1* or inhibition of clathrin-mediated endocytosis effectively prevented their internalization into cells (Extended Data Fig. 3a–c and Supplementary Fig. 4a), thereby hindering subsequent autophagy induction (Extended Data Fig. 2b and Supplementary Fig. 4b). These findings indicate that Atz-AUTAB triggers autophagy differently from PEI, likely because of differences in cellular uptake. Unlike PEI, which can enter cells through plasma membrane penetration or endocytosis[23], AUTABs enter cells exclusively by coendocytosis with target proteins. Therefore, PEI can trigger both LC3B-mediated autophagy, likely because of its cytosolic effect, and LC3C-mediated autophagy, attributed to its endosomal effect. Consistently, endocytosis inhibition only blocks PEI-triggered LC3C but not LC3B autophagosome formation (Supplementary Fig. 4c,d). In contrast, AUTABs induce only LC3C-mediated autophagy, specifically targeting endosomes containing their respective target proteins.

Through coimmunofluorescence staining with endosome markers, Rab5, Rab7 and AP2, we also demonstrated that the membrane damage and autophagy activation induced by Atz-AUTAB treatment both occurred on endosomes (Extended Data Fig. 4a–d and Supplementary Fig. 5a), which aligns with the reported LC3C-mediated autophagic mechanism[19]. These results were further validated by the triple colocalization of LC3C, galectin 3 and either Rab5 or Rab7 (Supplementary Fig. 5b,c). Expectedly, these damaged Atz-AUTAB-containing endosomes were eventually delivered to lysosomes for degradation (Supplementary Fig. 5d). Additionally, our research revealed that Atz-AUTAB-induced LC3C puncta exhibited colocalization with ATG9A, a crucial autophagy factor involved in cell membrane damage repair, in close proximity to the plasma membrane (Extended Data Fig. 5a). This suggests that the membrane injury originated from the cell surface. This was confirmed by a propidium iodide (PI) uptake assay, where cells treated with 100 nM Atz-AUTAB exhibited plasma membrane leakage compared to PEI and Atz treatment groups (Extended Data Fig. 5b). These data combined demonstrate a causal relationship between membrane damage and autophagy activation.

We finally investigated the use of Atz-AUTAB to remove cell surface PDL1. Immunofluorescence staining showed that Atz-AUTAB treatment substantially reduced surface HA–PDL1, unlike PEI or Atz treatments (Fig. 2g). Further flow cytometry confirmed an ~10-fold decrease in HA–PDL1 levels on the cell surface with Atz-AUTAB (Fig. 2h). This effect was also observed on endogenous PDL1 in MAD-MB-231 cells. Our data showed that Atz-AUTAB treatment progressively reduced cell surface PDL1 levels: ~25% reduction at 30 min, ~40% at 2 h and ~80% after 24 h (Fig. 2i).

Notably, PEI's transmembrane delivery capability enabled Atz-AUTAB to undergo endocytosis 2–3 times faster than Atz (Extended Data Fig. 3d). Accompanied by this, the internalization of PDL1 was also greatly facilitated by Atz-AUTAB (Extended Data Fig. 3e). These results suggest that AUTAB uses an additional endocytic mechanism before inducing autophagy, thereby aiding the autophagic degradation of plasma membrane proteins.

Degradation of PDL1 by Atz-AUTAB

We next used western blotting to assess PDL1 degradation after treating MDA-MB-231 cells with Atz-AUTAB for 24 h. Atz-AUTAB significantly reduced the total PDL1 level, whereas Atz alone or combined with a twofold concentration of PEI did not affect PDL1 level. PEI alone, even at 16 times the concentration of Atz-AUTAB, also had no impact on PDL1 turnover (Fig. 3a and Supplementary Fig. 6a). Reverse transcription (RT)–PCR results confirmed that the transcription level of *CD274*, which encodes PDL1, remained unchanged, supporting that PDL1 turnover was because of protein degradation (Supplementary Fig. 7). This degradation was dose dependent, beginning at 0.09 nM and peaking at 6.25 nM Atz-AUTAB (Fig. 3b and Supplementary Fig. 15). Time-wise, Atz-AUTAB started to degrade PDL1 at 12 h after treatment and nearly eliminated the PDL1 signal after 24 h (Fig. 3c and Supplementary Fig. 15). These effects were also confirmed in HeLa cells stably expressing HA–PDL1 (Extended Data Fig. 6a–c and Supplementary Figs. 6b and 15) and in various cancer cell lines, suggesting the broad applicability of AUTAB degraders (Fig. 3d).

To confirm that Atz-AUTAB degrades PDL1 through the autophagic–lysosomal pathway, MDA-MB-231 cells were treated with lysosome inhibitors bafilomycin A1 and chloroquine. Both inhibitors blocked PDL1 degradation by Atz-AUTAB (Fig. 3e and Extended Data Fig. 6d). Furthermore, combining Atz-AUTAB with these inhibitors further stabilized PDL1 compared to using the inhibitors alone. These findings suggest that the degradation profile of PDL1 was altered under these conditions, potentially leading to an increased shift of PDL1 toward lysosomal degradation from proteasomal degradation. Furthermore, in line with expectations, knockdown of *LC3C* but not *LC3B* significantly inhibited the Atz-AUTAB-induced PDL1 degradation, although not entirely (Fig. 3f and Extended Data Fig. 6e,f). Contrary to our expectation, however, *LC3C* knockout did not demonstrate a rescue effect (Extended Data Fig. 6g). Interestingly, under these conditions, GABARAPs, a different subfamily of ATG8 proteins, were upregulated (Extended Data Fig. 6g), indicating a compensatory role of these proteins. Indeed, codeleting GABARAPs, including *GABARAP*, *GABARAPL1* and *GABARAPL2*, with *LC3C* knockout nearly completely rescued Atz-AUTAB-induced PDL1 degradation (Fig. 3g), whereas silencing any individual protein had no impact (Extended Data Fig. 6h). This dual depletion also reduced lysosomal delivery of AUTAB-damaged endosomes (Extended Data Fig. 6i), indicating a disruption of autophagy in this scenario. In agreement to these data, depletion of *ATG4B* and *ATG5*, two upstream genes of *ATG8*, also largely rescued the PDL1 degradation induced by AUTAB (Fig. 3h and Extended Data Fig. 6j). Notably, the degradation of PDL1 by Atz-AUTAB is also endocytosis dependent, as the endocytosis inhibitor dynasore effectively prevented this degradation (Supplementary Fig. 8). Together, these data support that AUTAB engages the autophagic–lysosomal pathway to degrade the target protein.

We then evaluated the degradation specificity in response to Atz-AUTAB treatment by performing a quantitative MS. As shown, PDL1 was the most significantly downregulated protein in cells treated with Atz-AUTAB, with no other proteins showing similar reduction levels, indicating the high selectivity of the AUTAB degrader (Fig. 3i). As a consequence of this suppression, several PDL1 signaling-related proteins were downregulated or upregulated weakly in Atz-AUTAB-treated cells (Supplementary Fig. 9a,b). Furthermore, the expression of some autophagy-related genes was altered in response to Atz-AUTAB treatment, providing unbiased confirmation of the autophagy dependent performance of the AUTABs (Supplementary Fig. 9a,b). Although canonical autophagy substrate p62 also undergoes lysosomal degradation (Supplementary Fig. 9c), it was not detected in the proteomic assay. This absence is likely attributed to its compensatory upregulation during autophagy (Supplementary Fig. 9d).

Subsequently, we investigated Atz-AUTAB's ability to deplete PDL1 in vivo by administering 5 mg kg^{-1} Atz-AUTAB intravenously to mice with MDA-MB-231 tumors for 3 days. Tumor analysis showed a significant reduction in PDL1 expression in the Atz-AUTAB group compared to the vehicle-treated or Atz-treated groups (Fig. 3j), thus suggesting the in vivo targeted degradation capability of AUTAB technology.

After studying Atz-AUTAB's degradation activity, we explored its potential for targeting PDL1 in antitumor immunotherapy. In an in vitro T cell-mediated tumor cell-killing assay, pretreatment with Atz-AUTAB or Atz restored T cell activity and enhanced tumor killing similarly. However, Atz-AUTAB was effective at a concentration at least four times lower than Atz, suggesting a stronger impact on immune checkpoint blockade for immunotherapy (Supplementary Fig. 10).

As AUTABs can harm cell membranes, we examined whether they also impact intracellular organelles. Our study found that Atz-AUTAB treatment did not affect cell viability, morphology, quantity or membrane integrity of key organelles (Supplementary Fig. 11a–e). Additionally, bulk RNA sequencing (RNA-seq) analysis indicated no significant stress signaling from organelle damage, unlike PEI, which induces oxidative stress (Supplementary Fig. 11f). Overall, these results suggest that AUTAB treatment is safe for organelles at working concentrations.

Expansion of AUTAB-addressable targets

To demonstrate the generality of the AUTAB modality, we applied it to degrade other plasma membrane proteins, including epidermal growth factor receptor (EGFR), a known therapeutic target in multiple cancers[24]. The AUTAB degrader for human EGFR was created by linking L25K PEI to the FDA-approved EGFR-blocking antibody cetuximab (Ctx). The conjugation efficiency was confirmed using denaturing gel electrophoresis (Extended Data Fig. 7a).

As shown, Ctx-AUTAB administration significantly reduced cell surface EGFR (Extended Data Fig. 7b,c). Similar to Atz-AUTAB, Ctx-AUTAB also induced significant LC3C-mediated autophagy that was accompanied by EGFR endocytosis (Fig. 4a and Extended Data Fig. 7d). Consistent with the autophagy machinery, endocytosed EGFR was observed to undergo lysosomal degradation (Extended Data Fig. 7e,f). The efficacy of EGFR degradation by Ctx-AUTAB was

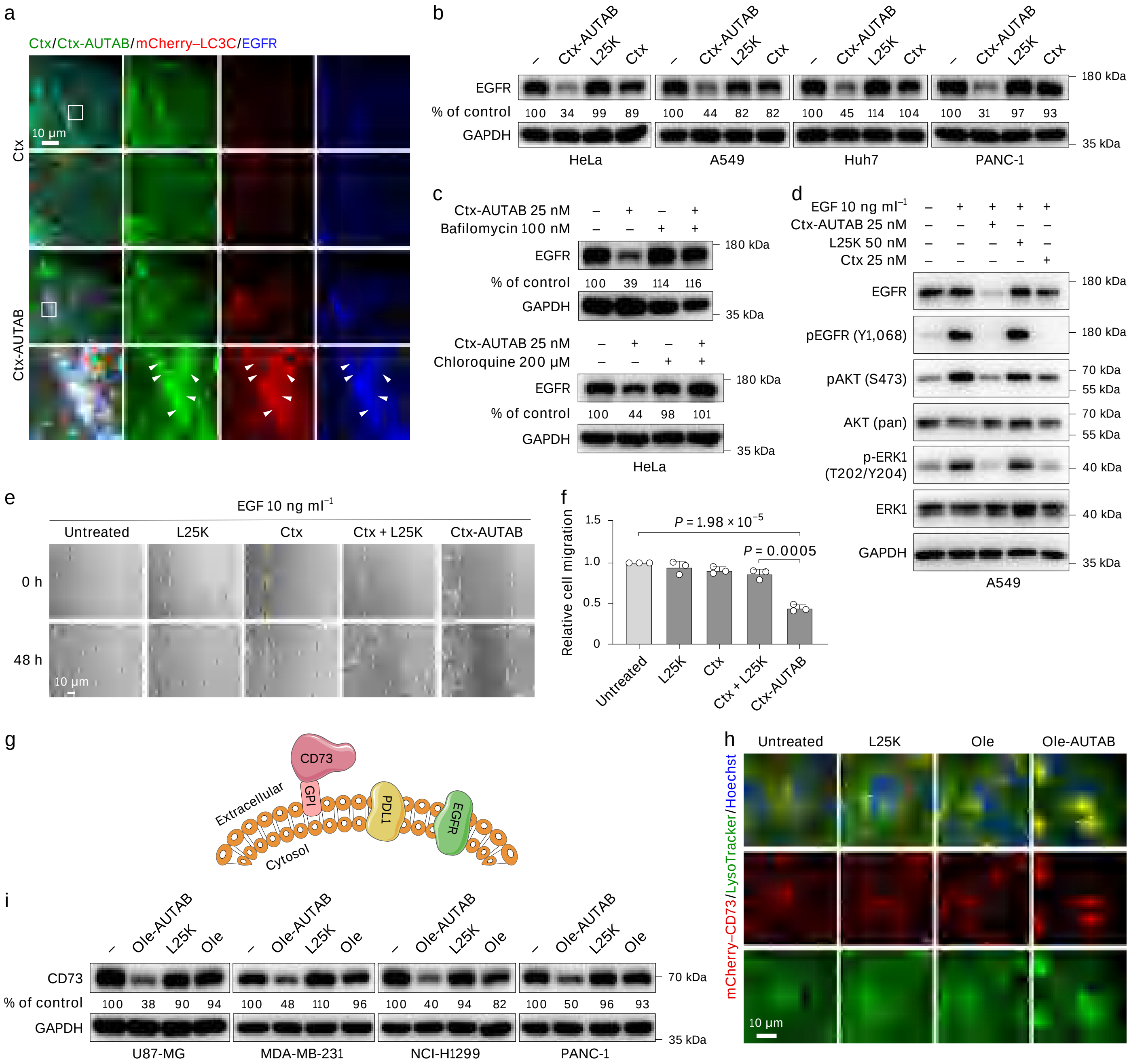

Fig. 4 | Degradation of EGFR and CD73 by AUTABs. a, HeLa cells stably expressing mCherry–LC3C were treated with 100 nM Ctx or Ctx-AUTAB for 1 h. Cells were then fixed, costained with antibodies to Ctx and EGFR and imaged by confocal microscopy. Bottom: enlarged views of the boxed regions. The arrowheads indicate the colocalization of Ctx-AUTAB, mCherry–LC3C and EGFR. **b**, Western blot analysis of total EGFR level in HeLa, A549, Huh7 and PANC-1 cells upon treatment with 50 nM L25K PEI, 25 nM Ctx or 25 nM Ctx-AUTAB, respectively, for 24 h. **c**, HeLa cells were treated with Ctx-AUTAB in the presence or absence of bafilomycin A1 or chloroquine for 24 h at the indicated concentrations. Cells were then harvested to detect the EGFR protein level through immunoblotting. **d**, Total and phosphorylated levels of EGFR, Akt and ERK in A549 cells were examined after 24 h of treatment with the indicated concentrations of L25K PEI, Ctx or Ctx-AUTAB. At 30 min before harvest, cells were further treated with 10 ng ml^{-1} EGF to stimulate EGFR downstream signaling. **e**, Wound-healing assay in PANC-1 cells pretreated with 100 nM L25K PEI, 50 nM Ctx, a Ctx–L25K PEI mixture or 50 nM Ctx-AUTAB for 12 h, and then incubated with 10 ng ml^{-1} EGF for 48 h. The yellow dashed lines indicate the wound edges at 0 h. **f**, Quantification of the cell migration in **e** ($n = 3$ biological replicates, means ± s.d.). **g**, Schematic of the types of plasma-membrane-associated proteins: (I) transmembrane proteins, such as PDL1 and EGFR, and (II) membrane-anchored proteins, such as CD73. **h**, HeLa cells stably expressing mCherry–CD73 were treated with 200 nM L25K PEI, 100 nM Ole or 100 nM Ole-AUTAB for 12 h. Cells were then stained with LysoTracker green DND-26 followed by live-cell imaging with confocal microscopy. **i**, Western blot analysis of total CD73 levels in U87-MG, MDA-MB-231, NCI-H1299 and PANC-1 cells following treatment with 200 nM L25K PEI, 100 nM Ole or 100 nM Ole-AUTAB for 24 h. DNA in **h** was stained by Hoechst 33258. Scale bars, 10 μm (**a**,**h**) or 100 μm (**e**). Statistical significance was calculated using an unpaired two-tailed Student's *t*-test (**f**).

further confirmed in four cancer cell lines by immunoblotting (Fig. 4b). A detailed profile of EGFR degradation in HeLa cells further showed that Ctx-AUTAB had significant effects at 0.09 nM, with degradation starting at 6 h and peaking at 24 h (Extended Data Fig. 7g,h and Supplementary Fig. 15). Lastly, we showed that inhibition of lysosome activity with bafilomycin A1 or chloroquine prevented the Ctx-AUTAB-induced

EGFR degradation (Fig. 4c). Collectively, our data validated that the AUTAB platform could be applied to degrade EGFR.

After demonstrating the degradation capacity of Ctx-AUTAB on EGFR, we proceeded to investigate its biological activities. First, we compared the impact of EGFR degradation on downstream signaling between Ctx-AUTAB and Ctx. Surprisingly, despite Ctx-AUTAB greatly reducing EGFR levels, it inhibited EGF-induced protein kinase B (AKT) and extracellular signal-regulated kinase 1 (ERK1) phosphorylation similarly to Ctx. This indicates that blocking EGF from binding to EGFR is enough to suppress downstream phosphorylation (Fig. 4d). Then, we performed wound-healing assays to assess the effect of EGFR degradation on cell migration. Unlike Ctx or PEI, which showed no impact, Ctx-AUTAB significantly impeded tumor cell migration (Fig. 4e,f). Taken together, these findings indicate that Ctx-AUTAB constitutes a promising therapeutic approach for targeting EGFR and merits further clinical investigation.

Having shown the degradation capacity of AUTABs on PDL1 and EGFR, both of which are transmembrane proteins, we proceeded to investigate the feasibility of the AUTAB approach for membrane-anchored proteins. To this end, we devised another AUTAB degrader targeting CD73, a newly emerging immunotherapeutic cancer target anchored on plasma membrane through glycosyl phosphatidylinositol, using a CD73-blocking antibody under clinical trial, oleclumab (Ole)[25] (Fig. 4g and Extended Data Fig. 8a). Similar to Atz-AUTAB and Ctx-AUTAB, Ole-AUTAB significantly promoted the CD73 trafficking through endolysosomal pathway (Fig. 4h and Extended Data Fig. 8b), thus eliminating the cell surface CD73 in a concentration-dependent, time-dependent and lysosome-dependent manner (Extended Data Fig. 8c–f and Supplementary Fig. 15). This degradation ability of Ole-AUTAB was further validated in various types of cancer cells (Fig. 4i). Altogether, our results strongly demonstrated the extensive applicability of the AUTAB platform for targeting different types of plasma membrane proteins.

Chemical mechanism of action of AUTAB

In light of the fact that all types of PEI tested in our study demonstrated adequate capacity to induce LC3C-mediated autophagy (Fig. 1i,j), we then aimed to explore their potential in developing AUTABs. To this end, we synthesized various Atz-conjugated AUTABs using PEI molecules with diverse structures and sizes. The resulting AUTABs were examined by denaturing gel electrophoresis (Extended Data Fig. 9a). Immunoblotting analysis revealed that these Atz-AUTABs, regardless of their different structures and sizes, exhibited comparable efficacy to degrade PDL1 (Fig. 5a,b and Supplementary Fig. 15). Furthermore, the respective AUTABs conjugated with L2.5K PEI were also effective in degrading EGFR and CD73 (Extended Data Fig. 9b,c and Supplementary Fig. 15). Together, these results demonstrate the generalizability of PEI molecules for AUTAB construction.

We next speculated that the cationic nature of PEI molecules is crucial for the targeted degradation ability of AUTABs. To test this, we created a low-charged AUTAB by conjugating Atz with partially acetylated (~65%) L2.5K PEI (Fig. 5c and Extended Data Fig. 9d). Compared to regular Atz-AUTAB, this low-charged Atz-AUTAB demonstrated a significantly diminished capacity to facilitate PDL1 endocytosis, autophagy initiation and PDL1 protein degradation (Fig. 5d–g, Extended Data Fig. 9e and Supplementary Fig. 15), indicative of a positive-charge-dependent mechanism of action of AUTAB. To further demonstrate this issue, we opted to substitute PEI with poly(L-lysine) (polyLys), a commonly used material in biomedical research because of its abundance of positive charges under physiological conditions, to generate AUTABs. We selected commercially available polyLys (4–15 or 15–30 kDa) to conjugate with Atz, aiming to assess its efficacy in eliciting targeted protein degradation (Supplementary Fig. 12 and Extended Data Fig. 9f). Notably, polyLys–Atz-AUTABs also induced robust autophagy, akin to Atz-AUTAB treatment (Fig. 5h and Extended Data Fig. 9g). Furthermore, two variants with different polyLys sizes degraded PDL1 as effectively as L25K PEI-conjugated Atz-AUTAB (Fig. 5i and Supplementary Fig. 15). These results combined demonstrate a positive charge dependency of AUTAB technology.

Development of secondary nanobody-based AUTABs

After demonstrating the chemical mechanism of action of AUTABs, we proceeded to investigate the feasibility of coupling PEI to target receptors using a general secondary antibody. Successful implementation of this approach would greatly streamline the AUTAB technology for targeting various plasma membrane proteins. However, attaching PEI to a secondary antibody might distance PEI from the target, potentially reducing AUTAB degradation efficiency. To circumvent this limitation, we opted to use a smaller nanobody and a smaller variant of PEI to construct a new type of AUTAB, referred to as nano-AUTAB, by conjugating maleimide-modified L2.5K PEI (L2.5K–MA) to cystine residues of a commercially available secondary nanobody capable of recognizing both human and rabbit IgG (Supplementary Fig. 13a). In principle, the nano-AUTAB could selectively degrade diverse plasma membrane proteins when used in conjunction with their specific primary antibodies (Fig. 6a). After confirming the conjugation of PEI and nanobodies using denaturing gel electrophoresis (Fig. 6b), the nano-AUTAB was initially used to degrade PDL1. As per our hypothesis, nano-AUTAB, with Atz, effectively cleared the cell surface PDL1, whereas nanobody without PEI tagging exhibited no discernible impact (Fig. 6c). Furthermore, nano-AUTAB could degrade PDL1 when paired with different primary PDL1 antibodies, including Atz and other research-grade PDL1 antibodies (Fig. 6d–f). Additionally, we successfully used the nano-AUTAB for the degradation of diverse plasma membrane proteins, including CD73 and integrin α5 (Fig. 6g,h). To test its versatility with different secondary nanobodies, we created nano-AUTAB-m using a commercially available secondary nanobody to mouse IgG (Supplementary Fig. 13b). Through degradation assays aimed at Flag–Notch1, which was exogenously expressed in human umbilical vein endothelial cells (HUVECs), we demonstrate that nano-AUTAB-m functioned effectively with the assistance of a mouse-derived anti-Flag antibody (Supplementary Fig. 13c). Together, these results provide comprehensive validation of the broad applicability and high efficacy of nano-AUTABs in both research and drug discovery. Notably, nano-AUTABs can degrade multiple targets simultaneously, as evidenced by the concurrent degradation of PDL1 and EGFR in MDA-MB-231 cells (Fig. 6i), offering a new strategy for developing multitargeting drugs for disease therapy.

We also attempted to use our nano-AUTAB technology to degrade multipass transmembrane protein. Regrettably, all tested proteins exhibited resistance to degradation (Supplementary Fig. 13d–f). This outcome suggests that AUTAB may not be efficacious for these proteins. Further research is required to determine whether this phenomenon is a prevalent characteristic of all existing membrane protein degradation technologies.

Pharmacokinetics and therapeutic potential of AUTAB in vivo

To investigate the therapeutic potential of AUTAB in vivo, we first used Atz-AUTAB as a model to evaluate its pharmacokinetics in mice. The results indicated a significant reduction in serum Atz-AUTAB level within 24 h after injection, with a minimal level remaining at 72 h (Supplementary Fig. 14a,b). This rapid clearance of AUTAB in vivo may be attributed to its positively charged properties. Further organ distribution analysis showed that Atz-AUTAB mainly accumulated in the liver and kidney 72 h after injection, suggesting that it was eliminated through hepatic metabolism and renal excretion (Supplementary Fig. 14c,d).

Subsequently, an animal experiment was conducted to evaluate the antitumor properties of AUTAB targeting PDL1 (Extended Data Fig. 10a). To avoid potential immunogenicity issues with the

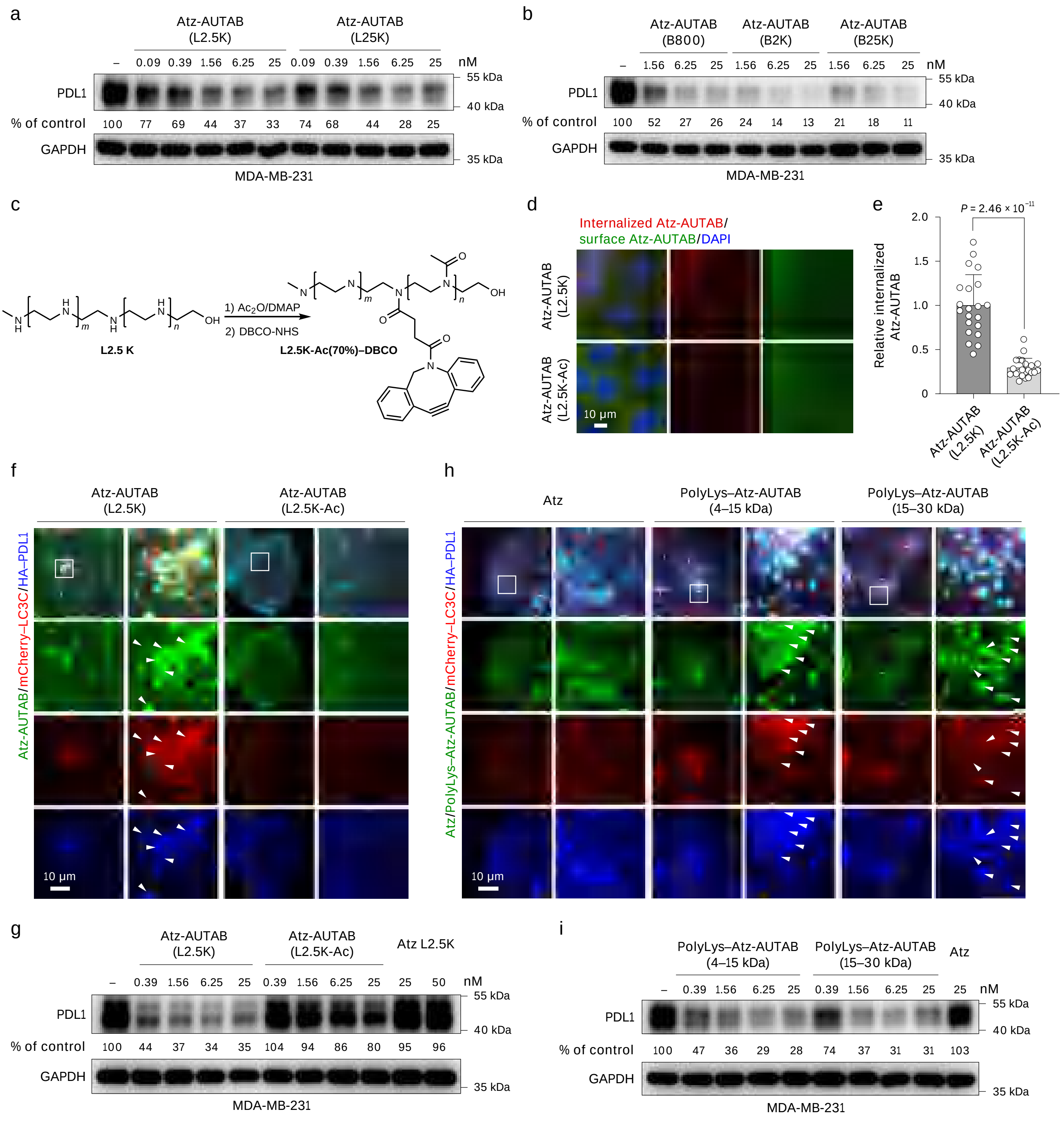

Fig. 5 | AUTAB's function depends on the cationic property of PEI. a,**b**, Western blot analysis of PDL1 degradation in MDA-MB-231 cells upon 24-h treatment with Atz-AUTABs conjugated with linear (**a**; L2.5K or L25K) or branched (**b**; B800, B2K or B25K) PEI as indicated. **c**, Synthesis of L2.5K-Ac–DBCO by partial acetylation (65%) of L2.5K PEI with Ac_2O and 4-dimethylaminopyridine and subsequent DBCO functionalization with DBCO-NHS at the molar ratio 1:1. **d**, Immunostaining images showing the internalizing efficacy of Atz-AUTABs (L2.5K or L2.5K-Ac) after 1 h of incubation at a concentration of 1 nM in HeLa cells stably expressing HA–PDL1. **e**, Quantification of internalized Atz-AUTABs (L2.5K or L2.5K-Ac) in **d** (Atz-AUTAB (L2.5K) group, *n* = 21 cells; Atz-AUTAB (L2.5K-Ac) group, *n* = 22; means ± s.d.). **f**, HeLa cells stably expressing HA–PDL1 and mCherry–LC3C were treated with 100 nM Atz-AUTABs (L2.5K or L2.5K-Ac) for 1 h. Cells were then fixed, costained with antibodies to Atz and HA and imaged. Right: enlarged views of the boxed regions. The arrowheads indicate the triple colocalization of Atz-AUTAB (L2.5K), mCherry–LC3C and HA–PDL1. **g**, Western blot analysis of PDL1 degradation in MDA-MB-231 cells incubated with increasing concentrations of Atz-AUTABs (L2.5K or L2.5K-Ac) for 24 h. **h**, HeLa cells concurrently expressing HA–PDL1 and mCherry–LC3C were treated with 100 nM Atz or polyLys–Atz-AUTABs (4–15-kDa or 15–30-kDa polyLys) for 1 h. Cells were then fixed, costained using antibodies to Atz and HA and imaged. Right: enlarged views of the boxed regions. The arrowheads indicate the triple colocalization of polyLys–Atz-AUTABs, mCherry–LC3C and HA–PDL1. **i**, Western blotting to detect the PDL1 degradation in MDA-MB-231 cells after 24-h treatment with increasing concentrations of polyLys–Atz-AUTABs. DNA in **d** was counterstained with DAPI. Scale bars, 10 μm. Statistical significance was calculated using an unpaired two-tailed Student's *t*-test (**e**).

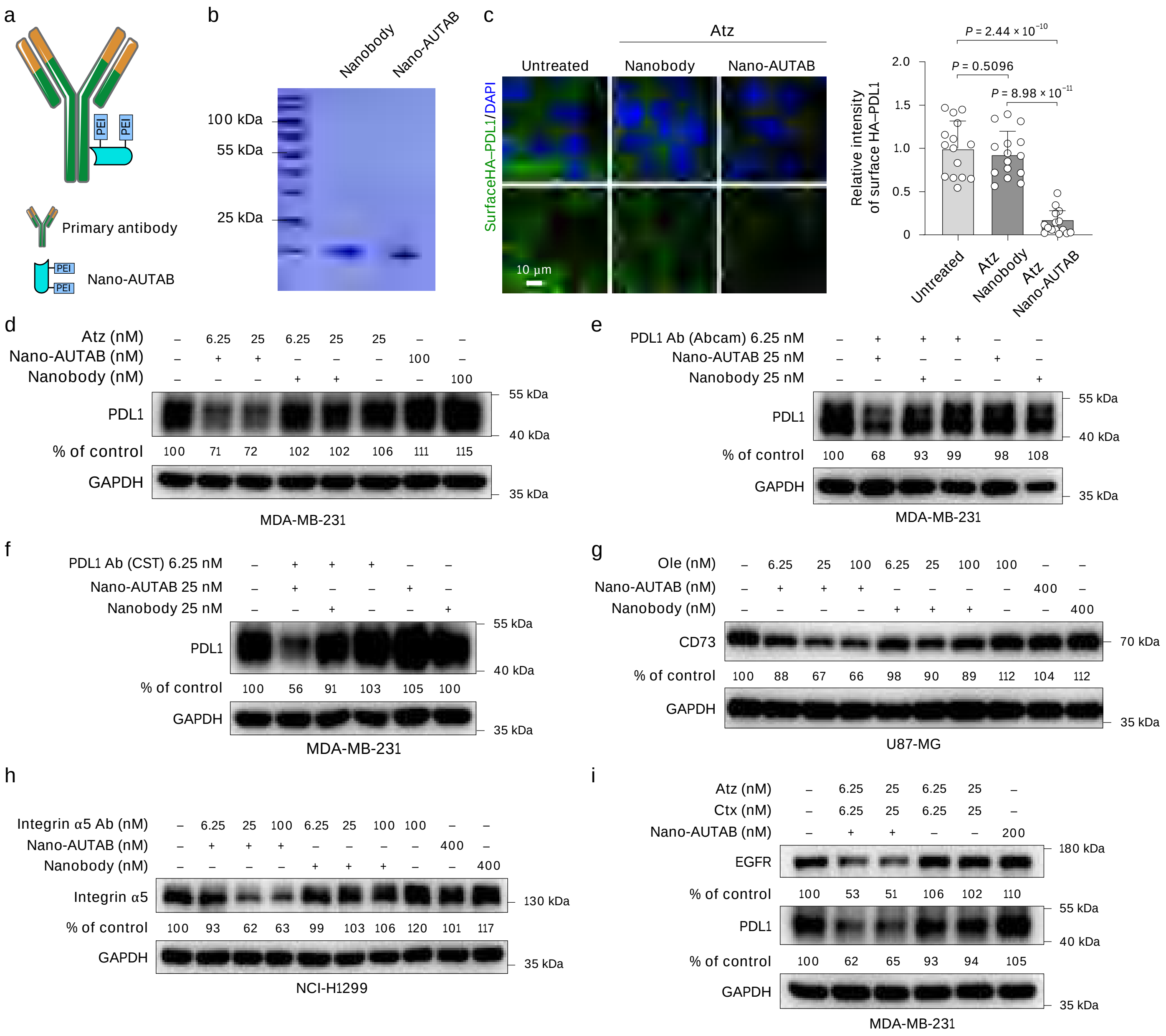

Fig. 6 | Development of secondary nanobody-based AUTABs. a, Schematic of the secondary nanobody-based AUTABs. **b**, SDS–PAGE analysis of the nano-AUTAB. **c**, Immunostaining and quantification for surface PDL1 in HeLa cells expressing HA–PDL1 treated with a combination of 6.25 nM Atz with 25 nM nanobody or 25 nM nano-AUTAB for 24 h ($n = 15$ cells, means ± s.d.). **d**–**f**, Western blot analysis of PDL1 in MDA-MB-231 cells treated with a combination of nano-AUTAB and the primary antibody Atz (**d**), PDL1 antibody from Abcam (**e**) or PDL1 antibody from Cell Signaling (**f**) for 24 h at the indicated concentrations. **g**, Western blot of CD73 in U87-MG cells treated with indicated antibodies for 24 h. **h**, Western blotting to detect the integrin α5 degradation in NCI-H1299 cells treated with indicated concentrations of nano-AUTAB and anti-integrin α5 antibody for 24 h. **i**, Western blot analysis of concurrent degradation of PDL1 and EGFR in MDA-MB-231 cells upon treatment with a combination of Atz, Ctx and nano-AUTAB for 24 h at the indicated concentrations. DNA in **c** was counterstained with DAPI. Scale bars, 10 μm. Statistical significance was calculated using an unpaired two-tailed Student's *t*-test (**c**).

humanized antibody Atz in mice with normal immune function, a separate AUTAB was developed for mouse PDL1 (mPDL1-Ab-AUTAB) (Extended Data Fig. 10b). Our data indicated that the mPDL1-Ab-AUTAB was well tolerated (Extended Data Fig. 10c) and effectively induced PDL1 degradation, enhanced T cell infiltration and inhibited MC38 tumor growth in C57BL/6J mice (Extended Data Fig. 10d–h). When compared to the antibody alone, however, the antitumor efficacy of AUTAB exhibited only marginal enhancement, likely because of the swift elimination induced by PEI conjugation. Hence, enhancing the metabolic stability of AUTAB is imperative for optimizing its therapeutic efficacy.

Discussion

Inspired by PROTACs, numerous degradation strategies have emerged to target plasma membrane proteins that are readily accessible as drug targets[7–12,26–33]. The majority of these strategies rely on the endolysosomal degradation pathway. While the high selectivity toward a particular protein could be achieved through specific antibodies, because of the poor understanding of the endocytic sorting mechanism, a desirable quick and direct delivery of the target protein to lysosomes remains undesignable. Autophagy is a known mechanism that can direct cargo for degradation through lysosomes quickly and directly[34]. Indeed, autophagy has been used for targeted protein degradation[14–16,35];

however, the current technologies are all confined to cytosolic components, because autophagy occurs only in the cytoplasm. Here, we successfully established a class of autophagy-based modality that is applicable for the targeted degradation of plasma membrane proteins. By leveraging antibodies covalently tagged with an autophagy-inducing chemical agent, PEI, we successfully direct plasma membrane proteins on the path to lysosomes for destruction through autophagic machinery. We term this technology AUTABs. Unlike most existing protein degraders that function by physically tethering the target protein to aimed protein degradation machines for destruction, AUTABs do not require a physical interaction with the intracellular autophagy machine, instead driving protein turnover by generating autophagy signals that can be monitored by intracellular autophagy machinery. In this manner, AUTABs eliminate cell surface receptors through intracellular autophagic machinery. In principle, any plasma membrane protein with an accessible extracellular domain is potentially suitable to be designated for autophagic degradation by AUTABs.

AUTABs are simpler to design and synthesize than current plasma membrane protein degradation platforms because they do not need to bind two targets simultaneously or meet strict enzyme activity requirements. They also demonstrate efficient degradation at nanomolar concentrations, performing as well as or better than existing technologies. Moreover, we showed that secondary nanobody-based AUTABs, when used in conjunction with primary antibodies, could function as well as regular AUTABs, providing a more universally applicable approach for targeted protein degradation. Additionally, secondary nanobody-based AUTABs allow for targeting multiple membrane proteins for degradation with a single degrader one at a time. Together, these unique advantages make AUTAB a powerful and versatile platform for plasma membrane protein degradation, suitable for various research and drug discovery applications.

The proteomic analysis revealed that AUTABs can achieve high selectivity toward their protein targets. However, the levels of proteins closely associated with autophagy do not demonstrate notable modifications. This finding ostensibly conflicts with the autophagic mechanism used by AUTABs, whereby the components of the autophagosome, such as p62, would be concurrently degraded with the AUTAB molecules and their target proteins. A plausible explanation for this observed discrepancy is that the degradation effect on these proteins is mitigated by a compensatory increase in protein expression during autophagy. This hypothesis was subsequently validated for p62. Following treatment with a lysosome inhibitor, there was a significant elevation in the protein levels of p62. This finding suggests that the degradation of autophagic proteins does indeed occur but it is masked by their increased expression during autophagy.

Despite the promising protein targeted degradation capabilities exhibited by the AUTAB molecule, its effectiveness in degrading proteins and treating tumors in animal models is limited because of rapid in vivo metabolism, leading to poor tumor targeting. Consequently, future research endeavors should prioritize enhancing the metabolic stability of AUTABs in vivo by screening for chemical compounds with improved metabolism, such as natural products and clinically approved drugs. This optimization is crucial for the eventual clinical translation of AUTAB technology.

In summary, we developed a novel autophagy-based modality for plasma membrane protein degradation, with broad applicability for both biological research and therapeutic drug discovery.

Online content

Any methods, additional references, Nature Portfolio reporting summaries, source data, extended data, supplementary information, acknowledgements, peer review information; details of author contributions and competing interests; and statements of data and code availability are available at https://doi.org/10.1038/s41589-024-01803-1.

References

1. Hu, Z. et al. The Cancer Surfaceome Atlas integrates genomic, functional and drug response data to identify actionable targets. *Nat. Cancer* **2**, 1406–1422 (2021).
2. Tozzoli, R. Receptor autoimmunity: diagnostic and therapeutic implications. *Autoimmun. Highlights* **11**, 1 (2020).
3. Yin, H. & Flynn, A. D. Drugging membrane protein interactions. *Annu. Rev. Biomed. Eng.* **18**, 51–76 (2016).
4. Santos, R. et al. A comprehensive map of molecular drug targets. *Nat. Rev. Drug Discov.* **16**, 19–34 (2017).
5. Ahn, G., Banik, S. M. & Bertozzi, C. R. Degradation from the outside in: targeting extracellular and membrane proteins for degradation through the endolysosomal pathway. *Cell Chem. Biol.* **28**, 1072–1080 (2021).
6. Alabi, S. B. & Crews, C. M. Major advances in targeted protein degradation: PROTACs, LYTACs, and MADTACs. *J. Biol. Chem.* **296**, 100647 (2021).
7. Banik, S. M. et al. Lysosome-targeting chimaeras for degradation of extracellular proteins. *Nature* **584**, 291–297 (2020).
8. Ahn, G. et al. LYTACs that engage the asialoglycoprotein receptor for targeted protein degradation. *Nat. Chem. Biol.* **17**, 937–946 (2021).
9. Caianiello, D. F. et al. Bifunctional small molecules that mediate the degradation of extracellular proteins. *Nat. Chem. Biol.* **17**, 947–953 (2021).
10. Cotton, A. D., Nguyen, D. P., Gramespacher, J. A., Seiple, I. B. & Wells, J. A. Development of antibody-based PROTACs for the degradation of the cell-surface immune checkpoint protein PD-L1. *J. Am. Chem. Soc.* **143**, 593–598 (2021).
11. Marei, H. et al. Antibody targeting of E3 ubiquitin ligases for receptor degradation. *Nature* **610**, 182–189 (2022).
12. Pance, K. et al. Modular cytokine receptor-targeting chimeras for targeted degradation of cell surface and extracellular proteins. *Nat. Biotechnol.* **41**, 273–281 (2023).
13. Mizushima, N. & Komatsu, M. Autophagy: renovation of cells and tissues. *Cell* **147**, 728–741 (2011).
14. Takahashi, D. et al. AUTACs: cargo-specific degraders using selective autophagy. *Mol. Cell* **76**, 797–810 (2019).
15. Li, Z. et al. Allele-selective lowering of mutant HTT protein by HTT–LC3 linker compounds. *Nature* **575**, 203–209 (2019).
16. Ji, C. H. et al. The AUTOTAC chemical biology platform for targeted protein degradation via the autophagy–lysosome system. *Nat. Commun.* **13**, 904 (2022).
17. Gao, X. et al. The association of autophagy with polyethylenimine-induced cytotoxicity in nephritic and hepatic cell lines. *Biomaterials* **32**, 8613–8625 (2011).
18. Lin, C. W., Jan, M. S. & Kuo, J. H. Autophagy-related gene expression analysis of wild-type and *atg5* gene knockout mouse embryonic fibroblast cells treated with polyethylenimine. *Mol. Pharm.* **11**, 3002–3008 (2014).
19. Coelho, P. P. et al. Endosomal LC3C-pathway selectively targets plasma membrane cargo for autophagic degradation. *Nat. Commun.* **13**, 3812 (2022).
20. Vargas, J. N. S., Hamasaki, M., Kawabata, T., Youle, R. J. & Yoshimori, T. The mechanisms and roles of selective autophagy in mammals. *Nat. Rev. Mol. Cell Biol.* **24**, 167–185 (2023).
21. Millarte, V., Schlienger, S., Kalin, S. & Spiess, M. Rabaptin5 targets autophagy to damaged endosomes and *Salmonella* vacuoles via FIP200 and ATG16L1. *EMBO Rep.* **23**, e53429 (2022).
22. Pied, N. et al. TBK1 is part of a galectin 8 dependent membrane damage recognition complex and drives autophagy upon adenovirus endosomal escape. *PLoS Pathog.* **18**, e1010736 (2022).
23. Casper, J. et al. Polyethylenimine (PEI) in gene therapy: current status and clinical applications. *J. Control. Release* **362**, 667–691 (2023).

24. Guardiola, S., Varese, M., Sanchez-Navarro, M. & Giralt, E. A third shot at EGFR: new opportunities in cancer therapy. *Trends Pharmacol. Sci.* **40**, 941–955 (2019).
25. Bendell, J. et al. First-in-human study of oleclumab, a potent, selective anti-CD73 monoclonal antibody, alone or in combination with durvalumab in patients with advanced solid tumors. *Cancer Immunol. Immunother.* **72**, 2443–2458 (2023).
26. Burslem, G. M. et al. The advantages of targeted protein degradation over inhibition: an RTK case study. *Cell Chem. Biol.* **25**, 67–77 (2018).
27. Miao, Y. et al. Bispecific aptamer chimeras enable targeted protein degradation on cell membranes. *Angew. Chem.* **60**, 11267–11271 (2021).
28. Zhang, H. et al. Covalently engineered nanobody chimeras for targeted membrane protein degradation. *J. Am. Chem. Soc.* **143**, 16377–16382 (2021).
29. Zhou, Y. X., Teng, P., Montgomery, N. T., Li, X. L. & Tang, W. P. Development of triantennary *N*-acetylgalactosamine conjugates as degraders for extracellular proteins. *ACS Cent. Sci.* **7**, 499–506 (2021).
30. Zheng, J. W. et al. Bifunctional compounds as molecular degraders for integrin-facilitated targeted protein degradation. *J. Am. Chem. Soc.* **144**, 21831–21836 (2022).
31. Wu, Y. et al. Aptamer-LYTACs for targeted degradation of extracellular and membrane proteins. *Angew. Chem. Int. Ed. Engl.* **62**, e202218106 (2023).
32. Zhu, C. H., Wang, W. S., Wang, Y., Zhang, Y. & Li, J. B. Dendronized DNA chimeras harness scavenger receptors to degrade cell membrane proteins. *Angew. Chem. Int. Ed. Engl.* **62**, e202300694 (2023).
33. Wang, K. et al. Nano-LYTACs for degradation of membrane proteins and inhibition of CD24/Siglec-10 signaling pathway. *Adv. Sci.* **10**, e2300288 (2023).
34. Gatica, D., Lahiri, V. & Klionsky, D. J. Cargo recognition and degradation by selective autophagy. *Nat. Cell Biol.* **20**, 233–242 (2018).
35. Fan, X., Jin, W. Y., Lu, J., Wang, J. & Wang, Y. T. Rapid and reversible knockdown of endogenous proteins by peptide-directed lysosomal degradation. *Nat. Neurosci.* **17**, 471–480 (2014).

Methods

Antibodies, reagents and primers

Comprehensive details regarding the antibodies, reagents, and RT–PCR primer sequences used in this study are provided in Supplementary Tables 1–3, respectively.

Chemical synthesis procedures

Azide-labeled antibodies were formed by the reaction of N_3-C5-NHS with the lysine residues of the antibodies. DBCO-functionalized PEIs were obtained by the reaction of DBCO-NHS with the amino groups of linear or branched PEIs. Maleimide-functionalized PEI was obtained by the reaction of *N*-succinimidyl 6-maleimidohexanoate (MA-C6-NHS) with the amino groups of linear PEI. AUTABs were generated through SPAAC between azide-labeled antibodies and DBCO-functionalized PEIs. Nano-AUTABs were generated through Michael-type addition reaction between the thiol groups of the nanobodies and maleimide-functionalized PEI. The Supplementary Note provides general and detailed synthetic procedures.

Gel analysis of AUTABs

The conjugation of PEI or polyLys to antibody was detected by SDS–PAGE. Equal amounts of AUTABs and antibodies were loaded and the electrophoresis was run for 120 min at 100 V. After electrophoresis, gels were then stained with Coomassie blue to visualize protein bands.

To monitor the N_3-C5-NHS-labeled antibody, agarose gel electrophoresis was performed. Samples were loaded into 1% agarose gel in histidine–MES buffer (100 mM histidine and 100 mM MES, pH 6.1) and electrophoresed at room temperature, with proteins visualized by Coomassie blue staining.

Cell lines

HeLa (CL-0101), MDA-MB-231 (CL-0150), U87-MG (CL-0238), A549 (CL-0016), PANC-1 (CL-0184), NCI-H292 (CL-0167), NCI-H1299 (CL-0165), NCI-H1975 (CL-0298), A375 (CL-0014), Huh7 (CL-0120) and HEK293T (CL-0005) cell lines were purchased from Procell Life Science and Technology. MC38 (STCC20018P) was purchased from Servicebio Life Science and Technology. All cell lines were cultured at 37 °C under 5% CO_2 in DMEM (Gibco, 11965126) supplemented with 10% FBS (Gibco, 10099141) and 1% penicillin–streptomycin (Gibco, 15140122).

Plasmids, small interfering RNAs and transfection

Human *CD274* and *NT5E* complementary DNA (cDNA) open reading frame clones (HG10084-CM and HG10904-ACR) were purchased from Sino Biological. HA–PDL1 was constructed by inserting three tandem HA epitopes into full-length PDL1 between Asn236 and Glu237 and then subcloned into CD532A lentivirus vector. mCherry–CD73 was constructed by inserting mCherry downstream of the CD73 signal peptide sequence and subcloned into CD532A. mCherry–LC3B and mCherry–LC3C were constructed by inserting mCherry at the N termini of LC3B and LC3C, respectively, and subcloned into CD532B (a modified CD532A plasmid with a blasticidin resistance gene). EGFP–Rab5 was generated by cloning the full-length *RAB5A* gene into the pEGFP-C2 vector. RFP–Lamp1 (1817) was purchased from Addgene. The *LC3C*-knockout plasmid was constructed by cloning the single guide RNA (5′-GCGTCAGACCCTTCAAGCAGcgg-3′) into LentiCRISPR v2 (Addgene, 52961). The *ATG5*-knockout plasmid (L24480) was purchased from Beyotime biotechnology.

Transient transfection was performed with MegaTran 2.0 (OriGene, TT210002) according to the manufacturer's instructions. Cells were transfected in 24-well plates with 250 ng of plasmid and collected 24 h later.

The sequences of small interfering RNAs (siRNAs) used in this study are detailed in Supplementary Table 4. siRNA was transfected with Lipofectamine 3000 (Invitrogen, L3000015). MDA-MB-231 cells were treated with 50 nM siRNA for 48 h according to the manufacturer's instructions and then collected for further analysis.

Generation of stable cell lines

To establish stable expression of HA–PDL1, mCherry–LC3B, mCherry–LC3C and mCherry–CD73 cell lines, recombinant lentiviruses were obtained by cotransfecting the corresponding lentiviral vectors with helper plasmids (psPAX2 and pMD2.G) into HEK293T cells and then infecting HeLa cells for 48 h. After infection, HeLa cells were selected in the presence of puromycin (1 μg ml^{-1}) or blasticidin (10 μg ml^{-1}) for 1 week. Isolated cell clones were validated by immunoblotting.

For the generation of *ATG5*-knockout and *LC3C*-knockout cells, HEK293T cells were transfected with the corresponding CRISPR lentiviral vectors along with psPAX2 and pMD2.G. Then, 48 h after transfection, supernatants containing the lentiviruses were collected and used to infect MDA-MB-231 cells. The infected cells were then selected and confirmed as described above.

HUVECs stably expressing Flag–Notch1 were established by similar method and described previously[36].

Immunoblotting

Cells were lysed with SDS lysis buffer (Beyotime biotechnology, P0013G) supplemented with protease inhibitor cocktail (MedChemExpress, HY-K0021). Lysates were centrifuged at 16,000*g* for 15 min and the protein concentrations were measured by BCA assay. Equal amounts of protein were separated by SDS–PAGE and transferred to the PVDF membrane for immunoblot analysis. The membrane was blocked and incubated overnight at 4 °C with primary antibodies and then treated with horseradish peroxidase (HRP)-conjugated secondary antibodies for 1 h at room temperature. Immunoblots were visualized with the Amersham Imager 600 system (GE Healthcare, Amersham Imager 600 operation software) and analyzed with ImageJ software to quantify band intensities. Protein levels were normalized to the reference glyceraldehyde-3-phosphate dehydrogenase or α-tubulin and presented as the relative expression levels compared to the control group.

Immunostaining

Cells were seeded on glass coverslips in 24-well plates 1 day before the experiment. After treatment with agents as indicated, the cells were fixed with 4% paraformaldehyde for 15 min, permeabilized with 0.2% Triton X-100 for 10 min and then blocked in blocking buffer (PBS and 3% BSA) for 30 min. Next, cells were sequentially incubated with primary antibodies and fluorescence-conjugated secondary antibodies for 2 and 1 h, respectively. Nuclei were stained with DAPI at the same time as secondary antibodies. For cell surface staining, cells were fixed and stained with antibodies under nonpermeabilized conditions.

Receptor internalization assay

The antibody feeding-based internalization assay was modified from our previously reported method[36]. Briefly, HeLa cells expressing HA–PDL1 were seeded on coverslips and incubated with mouse anti-HA primary antibodies for 1 h at 4 °C. After washing three times with cold PBS to remove the unbound antibodies, the cells were treated with Atz-AUTAB at 37 °C for indicated time periods. The cells were then fixed with 4% paraformaldehyde and a saturated Alexa Fluor 488-conjugated anti-mouse secondary antibody was used to label the remaining antibody-labeled receptor on the surface. Following permeabilization with 0.2% Triton X-100, the internalized antibody-labeled receptor was labeled with Alexa Fluor 555-conjugated anti-mouse secondary antibodies.

AUTAB uptake assay

The AUTAB uptake assay was similar to the experimental procedure described above. Cells were incubated with Atz-AUTAB at 37 °C for 1 h directly. Then, cells were washed on ice and fixed immediately.

The surface-remaining Atz-AUTAB was labeled with DyLight 488-conjugated goat anti-human secondary antibodies. The internalized Atz-AUTAB was stained with DyLight 550-conjugated goat anti-human secondary antibodies in a permeabilized condition.

PI uptake assay

The PI uptake assay was conducted to detect the changes in plasma membrane permeabilization as described previously[37]. Cells were incubated with 50 μg ml^{-1} PI and Hoechst 33258 for 10 min at 37 °C following treatment with the indicated concentrations of L25K PEI, Atz and Atz-AUTAB. After PI incubation, the samples were washed with PBS, fixed with 4% PFA and imaged by the Olympus IX81 microscope with a ×10 objective.

Cell viability assay

MDA-MB-231 cells were seeded into 96-well plates at a concentration of 5×10^4 cells per well and cultured overnight. Then, the cells were treated with L25K PEI or Atz-AUTAB for 24 and 48 h, respectively. Subsequently, 10 μl of CCK-8 solution was added to each well and incubated for 2 h at 37 °C. The optical density value at 450 nm was then measured using a microplate reader (Thermo).

Image acquisition and quantification

Cells were imaged using a Leica SD AF confocal microscope equipped with a ×63 (Plan apochromat, numerical aperture 1.4) oil immersion objective. Confocal Z-stack images were taken at 0.4-μm intervals and presented as maximum intensity projections (MIPs) using Leica MM AF software or Imaris software (Bitplane). Images were acquired under identical conditions for all comparisons.

Quantification of the fluorescence intensity was performed using Leica MM AF software. For internalized signal intensity measurements, the cell region was defined by outlining surface-staining signals in MIP images. The intensities of the internalized signal were then determined by calculating the integrated fluorescence intensity in each cell after subtracting the background intensity.

Colocalization analysis was performed using Imaris software. Using the 'spot' application, protein puncta were identified on the basis of intensity and size thresholds and a spot mask was created for each channel. The colocalized spots from different channels were defined if their distance was found within the diameter of the spot.

Flow cytometric analysis of cell surface PDL1, EGFR and CD73

Cells in 12-well plates were treated with different AUTABs or controls, harvested by trypsinization and washed with ice-cold fluorescence-activated cell sorting buffer (PBS and 2% FBS). Live cells were stained with primary antibody to the extracellular domain of PDL1 or EGFR for 30 min on ice, washed and then incubated with secondary antibody for 30 min on ice. For CD73, live HeLa cells stably expressing mCherry–CD73 were stained with anti-mCherry antibody, followed by incubation with Alexa Fluor 488-conjugated secondary antibody. The cells were analyzed by flow cytometry (CytoFLEX with CytExpert software, Beckman Coulter). Cell surface PDL1, EGFR or mCherry–CD73 signal was quantified using FlowJo software. The gating strategy is provided in Supplementary Fig. 16.

T cell-mediated tumor cell-killing assay

Human T cells (peripheral blood mononuclear cells, purchased from Milestone Biological Science and Technology, with approval by the Medical Ethics Committee of Zhoushan Putuo District People's Hospital (2021015KY)) were cultured in lymphocyte serum-free medium KBM 581 (Corning, 88-581-CM) supplemented with 10% FBS and 100 IU per ml interleukin 2 and prestimulated by 60 ng ml^{-1} anti-CD3 antibody and 30 ng ml^{-1} anti-CD28 antibody for 48 h. The MDA-MB-231 breast cancer cells were pretreated with L25K PEI, Atz, Atz-AUTAB or a combination of L25K PEI and Atz for 8 h. Subsequently, T cells and MDA-MB-231 cells were cocultured at an effector-to-target ratio of 5:1 for an additional 24 h. The killing activity of T cells was evaluated using the CytoTox 96 nonradioactive cytotoxicity kit (Promega, G1780) through a lactate dehydrogenase assay.

To further evaluate tumor cell apoptosis, cocultures were performed using MDA-MB-231 cells that stably express GFP, enabling tumor cell easy discernment. After coincubation of MDA-MB-231-GFP cells with T cells as described above, the cell mixture was harvested, stained with annexin V–PE and 7-AAD (Vazyme, A213-01) and subjected to flow cytometric analysis of apoptosis. The gating strategy is provided in Supplementary Fig. 16.

To assess the activation of T cells, interferon-γ (IFNγ) secretion in T cells was analyzed. The cocultured cells as described above were treated with BD GolgiStop for the last 12 h, fixed and permeabilized with Cytofix/Cytoperm solution (BD Pharmingen) and stained with anti-human IFN-γ–APC and anti-human CD3–PE. Then cells were analyzed by flow cytometry. The gating strategy is provided in Supplementary Fig. 16.

Animal models

All animal experiments were approved by the Institutional Animal Care and Use Committee of Shenzhen Institute of Advanced Technology. BALB/c nude mice (female, 6–8 weeks old) and C57BL/6J mice (female, 8 weeks old) were purchased from Beijing Vital River Laboratory Animal Technology and maintained under specific pathogen-free conditions with an ambient temperature of 24 ± 2 °C, air humidity of 40–70% and a 12-h light–dark cycle.

Pharmacokinetic study. BALB/c nude mice were intravenously injected with 5 mg kg^{-1} of Atz-AUTAB and blood samples were collected at 1, 6, 24, 48 and 72 h by tail bleed. Plasma was separated by centrifugation at 800*g* at 4 °C for 15 min. Organs (heart, liver, spleen, lung and kidney) were harvested at 72 h and lysed with radioimmunoprecipitation assay buffer containing protease and phosphatase inhibitors. Protein concentration was determined using a BCA kit and 30 μg of total protein was subjected to western blotting for the detection of human IgG Light chain.

PDL1 degradation in subcutaneous xenograft model. MDA-MB-231 cells (1×10^7) in 100 μL of PBS were subcutaneously inoculated into the right armpit of BALB/c nude mice. When the tumor volume reached approximately 50 mm^3, mice were randomly assigned to receive an intravenous injection of Atz-AUTAB or Atz antibodies at a dose of 5 mg kg^{-1} once daily for 3 days. The mice were killed 24 h after the last injection and the tumor tissues were collected for western blot analysis of PDL1.

Antitumor effect in syngeneic tumor model. MC38 cells (2.5×10^6) were mixed 1:1 with Matrigel (Corning, 354234) and subcutaneously injected into the right flanks of C57BL/6J mice. When tumors reached a mean volume of 100 mm^3 (5 days after inoculation), the mice were randomly divided into three groups ($n = 8$) and intravenously administered with PBS, mPDL1-Ab or mPDL1-Ab-AUTAB (5 mg kg^{-1}) on days 5, 8, 10, 12 and 14. Tumor volume and body weight were measured every 2–3 days. Tumor volume was calculated using the formula (length × width^2)/2. On day 16, tumor tissues were collected, weighed, imaged and randomly selected for the analysis of PDL1 protein levels and CD8$^+$ T cell infiltration.

Ex vivo fluorescence imaging. BALB/c nude mice were intravenously administered with Cy5.5-linked Atz-AUTAB at a dose of 5 mg kg^{-1}. Then, 72 h after injection, mice were killed and organ samples were collected and photographed. The fluorescence images were acquired using the IVIS Lumina system and analyzed by Living Image software.

Wound-healing assay

PANC-1 cells were seeded in 12-well plates, cultured up to 90–100% confluence and then starved with low-serum medium (1% FBS) containing L25K PEI, Ctx, Ctx-AUTAB or a combination of L25K PEI and Ctx for 12 h. Cell monolayers were scraped in a straight line with a pipette tip and washed with PBS. Cells were then incubated with the treatments plus 10 ng ml^{-1} EGF for 48 h. Cell migration into the scratched area was monitored using an Olympus IX81 live-cell imaging system equipped with a ×10 objective. Images were taken by xcellence rt software and quantified with ImageJ software. Cell migration was determined as follows: cell migration = area of wound (0 h) − area of wound (48 h), normalized to the untreated group.

Transmission electron microscopy

After 24-h treatment with L25K PEI, Atz or Atz-AUTABs, MDA-MB-231 cells were fixed in 2% paraformaldehyde and 2.5% glutaraldehyde for 3 h. Cells were then washed with 0.1 M phosphoric acid buffer (pH 7.0) and incubated in 1% osmic acid for 2 h. Subsequently, the cells were dehydrated using a graded ethanol series and embedded in Epon resins at 70 °C overnight. The samples were ultrathinly sliced with a microtome, stained with lead citrate for 10 min and uranyl acetate in 50% ethanol and imaged using a Hitachi HT7700 transmission electron microscopy instrument.

RNA-seq

RNA extraction and library construction. MDA-MB-231 cells were treated with L25K PEI, Atz or Atz-AUTAB for 24 h, followed by RNA extraction using a TRIzol kit (TIANGEN, DP424). RNA quality was assessed using agarose gel electrophoresis and spectrophotometry, selecting samples with a 260/280 ratio of 1.8–2.2 for library construction. mRNA-seq libraries were prepared using the Hieff NGS Ultima dual-mode mRNA library prep kit (Yeasen, 12309ES). cDNA was synthesized and amplified from the RNA, purified with the AMPure XP system (Beckman Coulter) and used for library construction. Fragments of 350–550 bp were enriched using PCR and library quality was assessed using an Agilent 2100 Bioanalyzer (Agilent). Sequencing was performed on the Illumina NovaSeq 6000 to produce 150-bp paired-end raw reads.

RNA-seq data and analysis. The raw data were filtered with TrimGalore to discard sequences containing adaptors and low-quality bases. The valid data obtained were then aligned against the hg19 human genome using HISAT2, followed by transcriptome data assembly and gene expression quantification using StringTie. Differentially expressed genes (DEGs) were identified by DEseq2 (for samples with replications) with a cutoff value of $\log_2$ |fold change| > 0.5 and P value < 0.05. The clusterProfiler tool was used to conduct functional enrichment analysis on the annotated significant DEGs, the potential genes in identified modules based on gene ontology categories.

Quantitative proteomic analysis

Sample preparation. Cells were treated with Atz or Atz-AUTAB for 24 h, washed with PBS, collected and frozen with liquid nitrogen. The frozen samples were lysed in lysis buffer (8 M urea and 1% protease inhibitor cocktail) with sonication. The supernatant was collected after centrifugation at 12,000*g* at 4 °C for 10 min. Protein concentration was measured with a BCA kit, followed by reduction with 5 mM dithiothreitol for 30 min at 56 °C and alkylation with 11 mM iodoacetamide for 15 min at room temperature for digestion. The sample was diluted to less than 2 M urea in 100 mM TEAB and peptides were digested with trypsin overnight at a mass ratio of 1:50 trypsin to protein. Finally, the peptides were desalted by the C18 SPE column.

Liquid chromatography–MS/MS analysis. Tryptic peptides were resuspended in buffer A (0.1% formic acid and 2% acetonitrile in water) and loaded onto a reversed-phase analytical column (25-cm length, 75/100-μm inner diameter). Peptides were separated by a gradient increasing from 6% to 24% buffer B (0.1% formic acid in acetonitrile) over 70 min, 24% to 35% in 14 min, climbing to 80% in 3 min and then maintaining at 80% for the last 3 min, all at a flow rate of 450 nl min^{-1} using a nanoElute ultrahigh-performance LC system (Bruker Daltonics). After elution, peptides were analyzed in parallel accumulation–serial fragmentation (PASEF) mode with a timsTOF Pro (Bruker Daltonics) at an electrospray voltage of 1.60 kV and an MS/MS scan range of 100–1,700 *m*/*z*. Peptide precursors with charge states of 0–5 were selected for fragmentation and ten PASEF MS/MS scans were acquired per cycle. The dynamic exclusion was set to 30 s.

Database analysis. The resulting raw data were processed using MaxQuant search engine and tandem mass spectra were searched against the full UniProt human database (20,422 entries) concatenated with a reverse protein sequence decoy database. Trypsin/P was specified as a cleavage enzyme that allows up to two missing cleavages. The mass tolerance was set as 20 ppm in the first search and 5 ppm in the main search for precursor ions, with 0.02 Da for the fragment ions. The false discovery rate was adjusted to <1%. Proteins were identified using at least one unique peptide and quantified according to label-free quantification intensity.

Statistics and reproducibility

Blots and gels in Figs. 1a,b, 2c, 3a,d–h, 4b–d,i and 6b,d–i, Extended Data Figs. 3b, 6a,d–h,j, 7a, 8a,f, 9a,b,d,f and 10b and Supplementary Figs. 2b, 6a,b, 8, 9c, 11e, 13b–f and 14d are representative of two independent experiments with similar results. Blots in Figs. 3b,c and 5a,b,g,i, Extended Data Figs. 6b,c, 7g,h, 8d,e and 9c and Supplementary Fig. 14a are representative of three independent experiments. Representative images shown in Figs. 1c–h,j, 2d–g, 4a,h, 5d,f,h and 6c, Extended Data Figs. 1b,c, 2b, 3c–e, 4a–d, 5a,b, 6i, 7b,e and 10h and Supplementary Figs. 1a,b, 3a–d, 4a–d, 5a–d and 11b–d were derived from at least three independent experiments. GraphPad Prism was used to perform statistical analysis. The values were expressed as the mean ± s.d. An unpaired two-tailed Student's *t*-test was used to compare the means between two groups. *P* values are indicated in the figures.

Reporting summary

Further information on research design is available in the Nature Portfolio Reporting Summary linked to this article.

Data availability

The data supporting the findings of this study are available within the paper and its Supplementary Information and in the ScienceDB repository (https://doi.org/10.57760/sciencedb.11745). The RNA-seq data generated in this study are available from the Gene Expression Omnibus database under accession code GSE279343. The proteomic raw data were deposited to the ProteomeXchange Consortium through the iProX repository with the dataset identifier PXD056766. The tandem mass spectra obtained from quantitative proteomic analysis were searched against the full UniProt human database. Source data are provided with this paper.

References

36. Shao, X. et al. Mammalian Numb protein antagonizes Notch by controlling postendocytic trafficking of the Notch ligand Delta-like 4. *J. Biol. Chem.* **292**, 20628–20643 (2017).
37. Claude-Taupin, A. et al. ATG9A protects the plasma membrane from programmed and incidental permeabilization. *Nat. Cell Biol.* **23**, 846–858 (2021).

Acknowledgements

We thank Z. Li for her help in plasmid preparation. This work was supported by grant 2023YFA0915400 (to L.C. and H.L.) from the

National Key R&D Program of China, grants 32371450 (to X.S.), 82304546 (to M.L.) and 21977111 (to L.F.) from the National Natural Science Foundation of China, grants 202381515040008 (to L.M. and H.L.), 2023A1515011765 (to L.F.) and 2021A1515012114 (to X.S.) from the Natural Science Foundation of Guangdong Province, grant 2020B1111540001 (to L.C.) from the Guangdong Provincial Key Area R&D Program, grants JCYJ20200109114608075 (to X.S.), JCYJ20210324120200001 (to H.L.) and JCYJ20210324101805014 (to K.L.) from the Shenzhen Science and Technology Program, grant D2301003 (to L.F.) from Shenzhen Medical Research Funds, grants JCYJ20220818100412028 (to L.F.) and JCYJ20220818101404010 (to L.F.) from the Shenzhen Fundamental Research Program and a grant from the SIAT Innovation Program for Excellent Young Researchers (to H.L.).

Author contributions

H.L., L.F., X.S. and L.C. conceptualized the project and supervised the study. B.C., M.L. J.L. and X.S. performed most of the cell biological, biochemical and animal experiments. J.Z., H.T. and L.F. synthesized and characterized the AUTAB conjugates. Y.L., Z.Z., L.D., W.S., W.Z. and K.L. participated in cell culture, immunofluorescence staining and flow cytometric analysis. R.L., J.R., H.H. and L.M. provided special technical support and discussed the data. B.C., M.L., X.S., L.F. and H.L. wrote the manuscript.

Competing interests

The authors declare no competing interests.

Additional information

Extended data is available for this paper at https://doi.org/10.1038/s41589-024-01803-1.

Supplementary information The online version contains supplementary material available at https://doi.org/10.1038/s41589-024-01803-1.

Correspondence and requests for materials should be addressed to Lintao Cai, Ximing Shao, Lijing Fang or Hongchang Li.

Peer review information *Nature Chemical Biology* thanks the anonymous reviewers for their contribution to the peer review of this work.

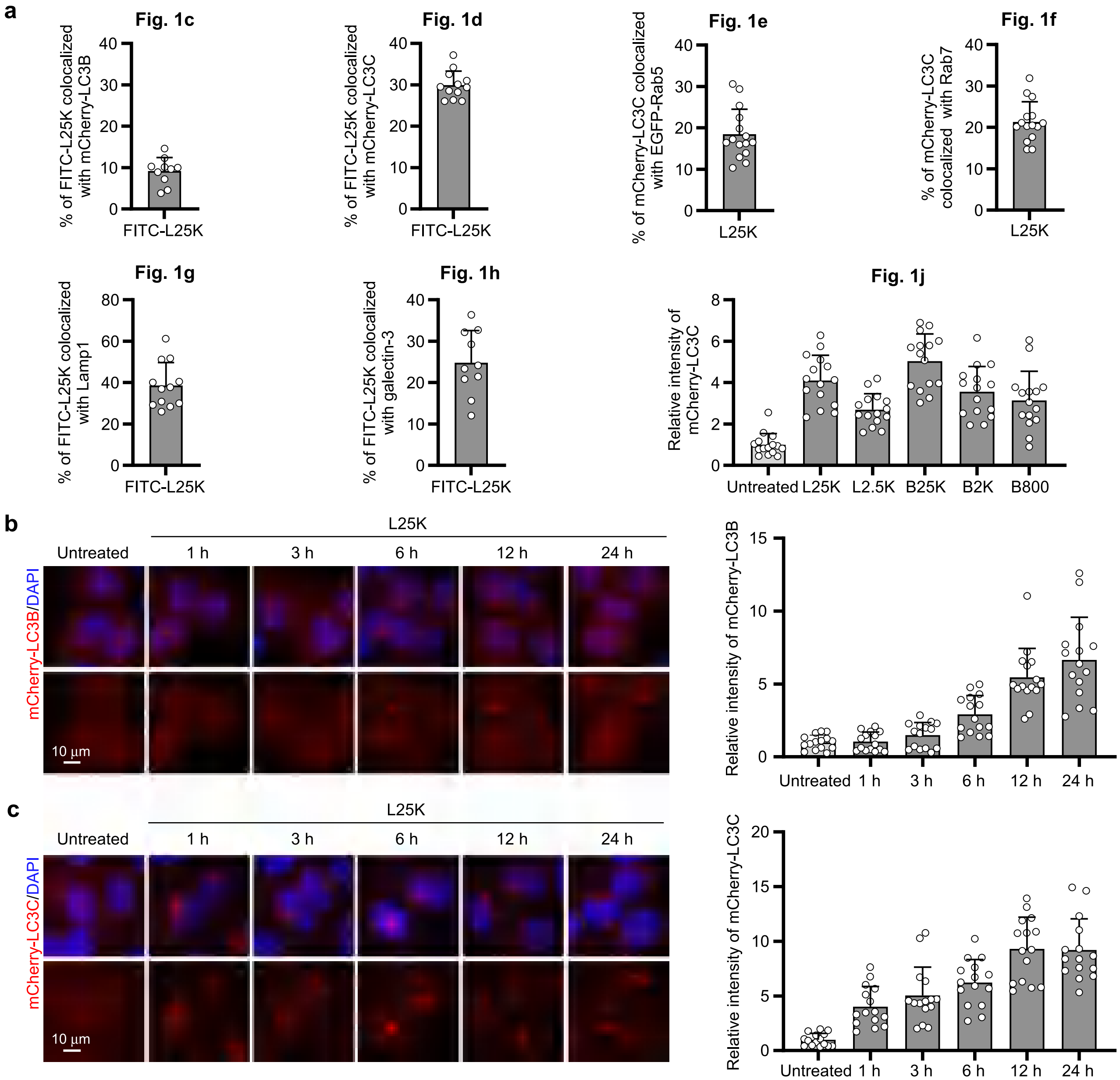

Extended Data Fig. 1 | Autophagy activation upon PEI treatment. a, The corresponding quantifications of confocal images in Fig. 1c–h and Fig. 1j (Fig. 1c, n = 10 cells; Fig. 1d, n = 12 cells; Fig. 1e, n = 15 cells; Fig. 1f, n = 15 cells; Fig. 1g, n = 12 cells; Fig. 1h, n = 10 cells; Fig. 1j, n = 15 cells, means ± s.d.; Quantification is unnecessary for the untreated group due to the absence of PEI signal in cell.). **b**,**c**, Representative images and relative quantifications of mCherry-LC3B (**b**) or mCherry-LC3C (**c**) stably expressing HeLa cells upon treatment with 1 μM of L25K PEI for indicated period of times. The quantifications are shown on the right (n = 15 cells per group, means ± s.d.). DNA in **b** and **c** was counterstained with DAPI. Scale bars, 10 μm.

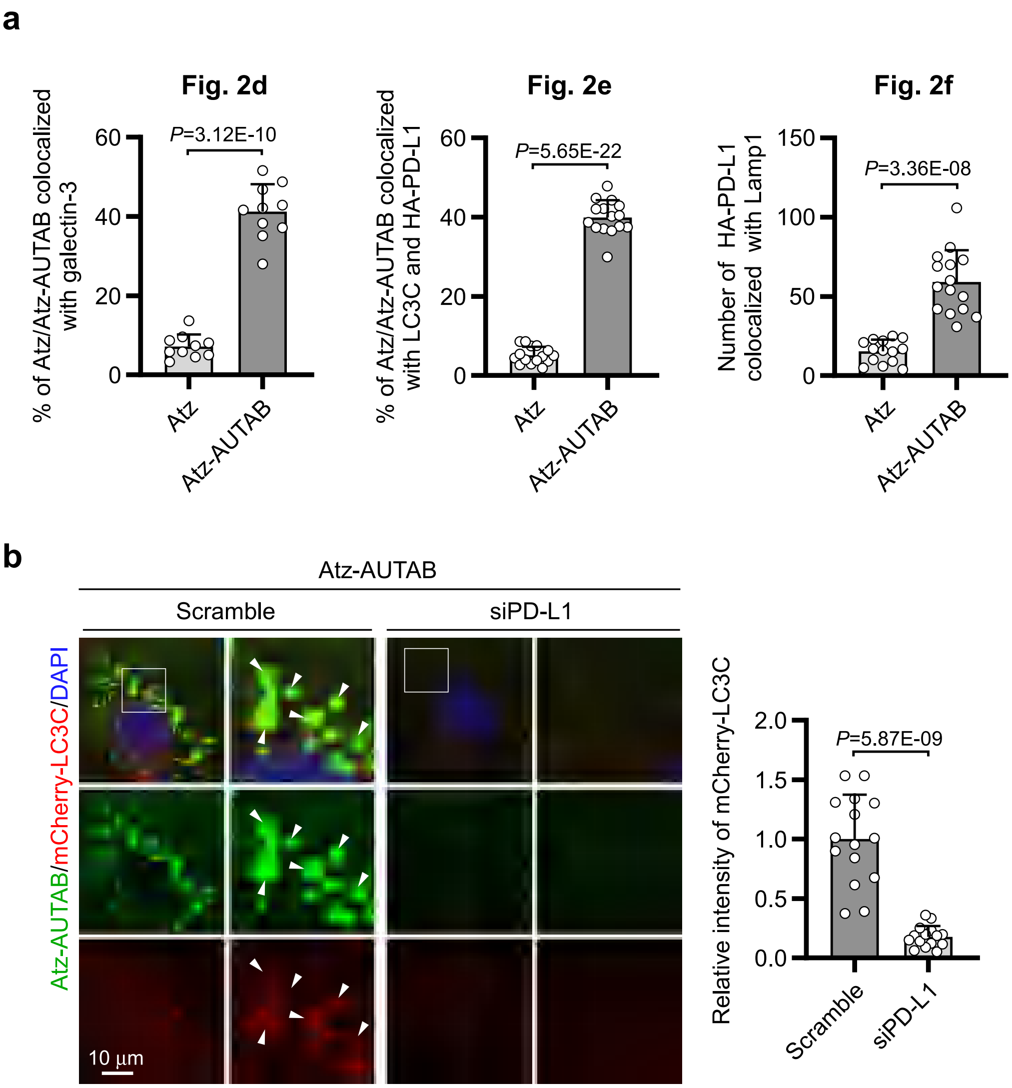

Extended Data Fig. 2 | AUTAB induces LC3C-mediated autophagy in a target receptor-dependent manner. a, The corresponding quantifications of confocal images in Fig. 2d–f (Fig. 2d, n = 10 cells per group; Fig. 2e, n = 15 cells per group; Fig. 2f, Atz group, n = 14 cells, Atz-AUTAB group, n = 15 cells, means ± s.d.). **b**, HA-PD-L1 and mCherry-LC3C expressing HeLa cells transfected with scramble or PD-L1 siRNA were incubated with 100 nM Atz-AUTAB for 1 h. Cells were then fixed, and stained with antibodies against Atz. Enlarged images of the white box are presented on the right, with arrowheads indicating the colocalization of mCherry-LC3C and Atz-AUTAB. The quantification is shown on the right of the panel (n = 15 cells per group, means ± s.d.). DNA in **b** was counterstained with DAPI. Scale bars, 10 µm. Statistical significance was calculated via unpaired two-tailed Student's *t*-test (**a**, **b**).

https://doi.org/10.1038/s41589-024-01803-1

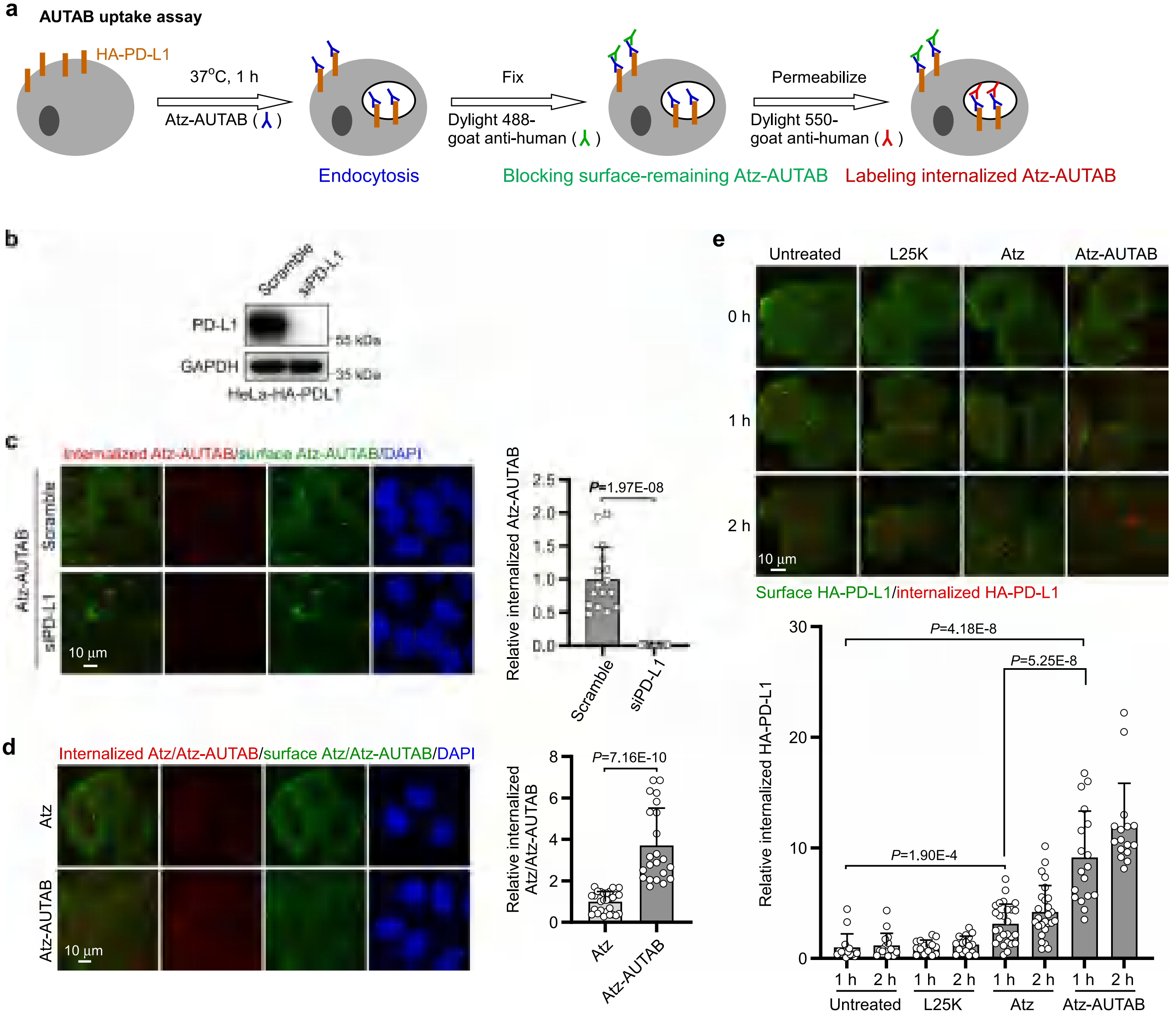

Extended Data Fig. 3 | Atz-AUTAB accelerates PD-L1 endocytosis. a, Schematic representation of Atz-AUTAB uptake assay (see Methods section for details). **b**, Confirmation by western blotting of PD-L1 knockdown in stable expressing HA-PD-L1 HeLa cells. **c**, HA-PD-L1 expressing HeLa cells with scramble or PD-L1 siRNA were incubated with 1 nM Atz or Atz-AUTAB for 1 h. After fixation, the surface-remaining and internalized Atz/Atz-AUTAB were sequentially stained before or after cell permeabilization. The fluorescence intensities of internalized Atz-AUTAB were quantified, and the data are expressed as each normalized value relative to the scramble group (scramble group, n = 16 cells; siPD-L1 group, n = 14, means ± s.d.). **d**, HA-PD-L1 expressing HeLa cells were incubated with 1 nM Atz or Atz-AUTAB for 1 h. After fixation, the surface-remaining and internalized Atz/Atz-AUTAB were sequentially stained before or after cell permeabilization. The quantification of the internalized Atz or Atz-AUTAB is shown on the right (Atz group, n = 28 cells; Atz-AUTAB group, n = 22; means ± s.d.). **e**, HeLa cells stably expressing HA-PD-L1 were subjected to antibody feeding-based internalization assay. Representative examples of internalized PD-L1 and surface-remaining PD-L1 are shown. The quantification of the internalized PD-L1 is shown below as indicated (untreated group, n = 15 cells for 1 h internalization, n = 16 for 2 h; L25K PEI group, n = 14 for 1 h, n = 17 for 2 h; Atz group, n = 27 for 1 h, n = 26 for 2 h; Atz-AUTAB group, n = 18 for 1 h, n = 16 for 2 h; means ± s.d.). DNA in **c** and **d** was counterstained with DAPI. Scale bars, 10 µm. Statistical significance was calculated via unpaired two-tailed Student's *t*-test (**c**-**e**).

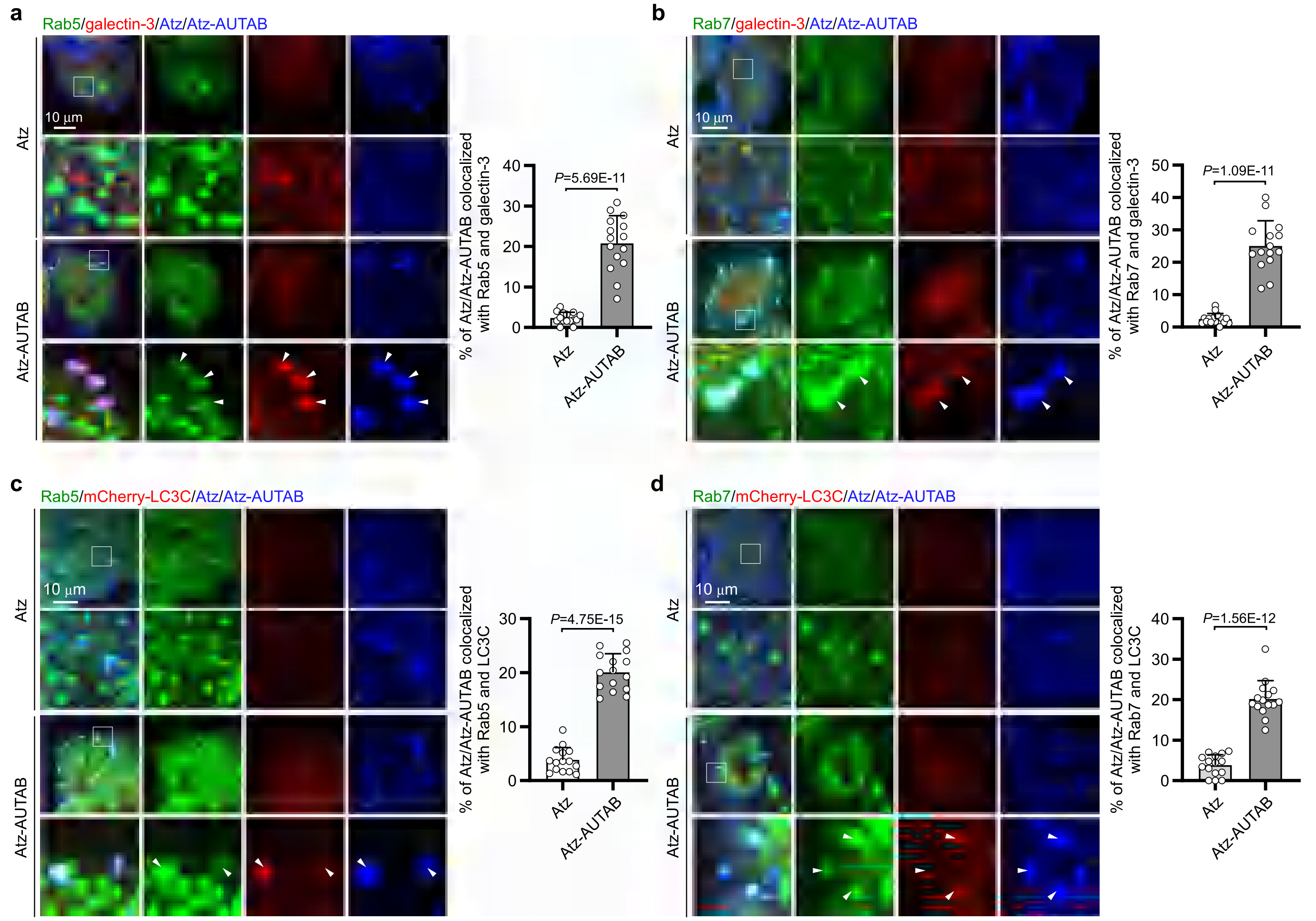

Extended Data Fig. 4 | Atz-AUTAB treatment damages endosome membrane and triggers LC3C-mediated autophagy. a,**b**, HeLa cells stably expressing HA-PD-L1 were treated with 100 nM Atz or Atz-AUTAB for 1 h. Cells were then fixed, co-stained using antibodies against galectin-3, Atz, and Rab5 (**a**) or Rab7 (**b**), and imaged by confocal microscopy. Enlarged views of the white boxed regions are shown below. The arrowheads indicate the triple colocalization of galectin-3, Atz-AUTAB, and Rab5 or Rab7. The relative quantification is shown on the right (n = 15 cells per group, means ± s.d.). **c**,**d**, HeLa cells concurrently expressing HA-PD-L1 and mCherry-LC3C were treated with 100 nM Atz or Atz-AUTAB for 20 min. After fixation, cells were co-stained with antibodies against Atz and Rab5 (**c**) or Rab7 (**d**), followed by confocal microscopy imaging. The white boxed regions are magnified below. The arrowheads indicate the colocalization of mCherry-LC3C and Atz-AUTAB on either early (Rab5-positive) or late (Rab7-positive) endosomes. The quantification is shown on the right (n = 15 cells per group, means ± s.d.). Scale bars, 10 µm. Statistical significance was calculated via unpaired two-tailed Student's *t*-test (**a**-**d**).

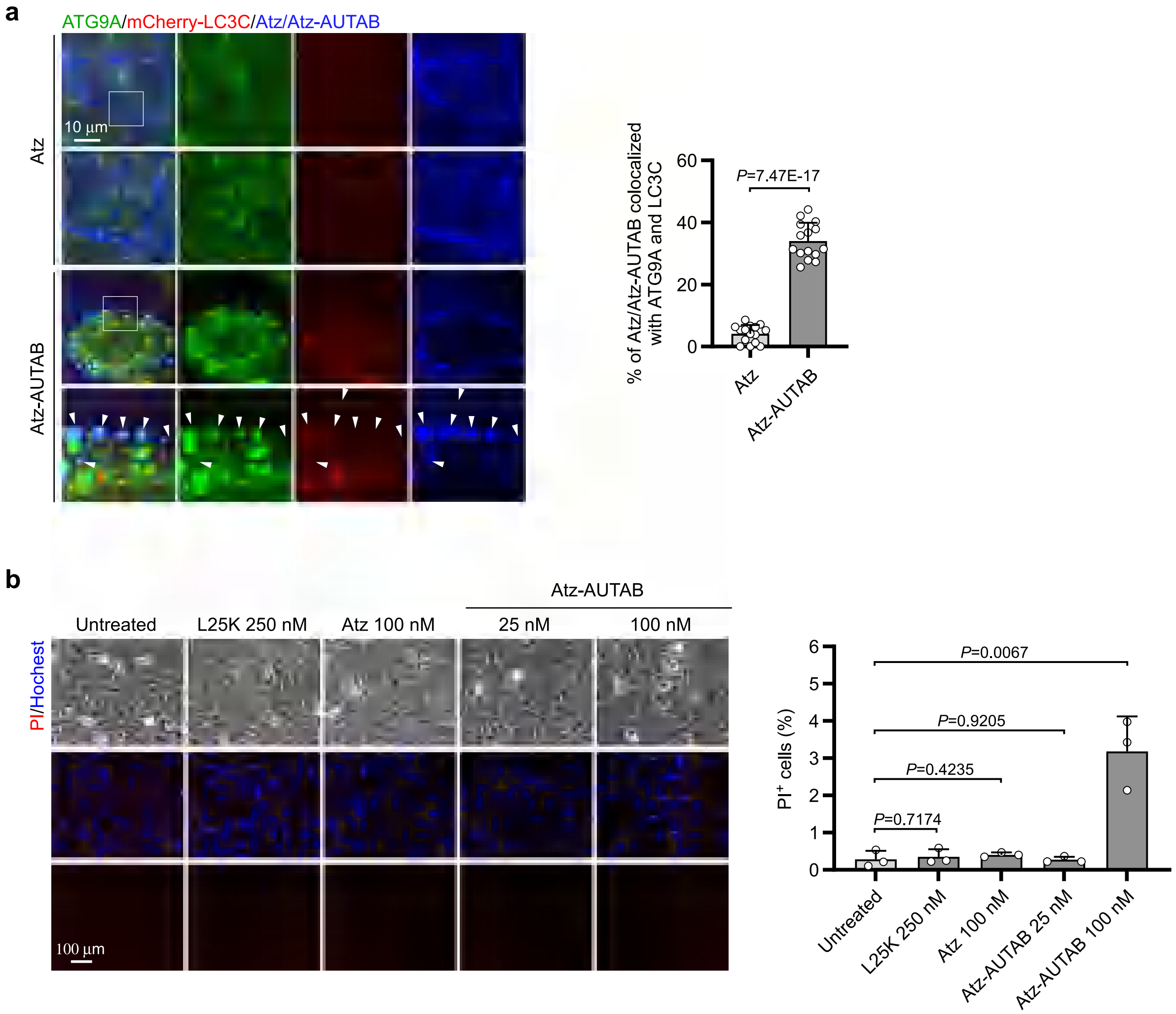

Extended Data Fig. 5 | AUTAB induces membrane damage at cell surface. **a**, Over-expressing HA-PD-L1 and mCherry-LC3C HeLa cells were treated with 100 nM Atz or Atz-AUTAB for 1 h, then fixed and co-stained with antibodies against ATG9A and Atz. Images were taken by confocal microscopy. The white boxed regions in the images are enlarged below and the arrowheads point to the colocalization between ATG9A, mCherry-LC3C and Atz-AUTAB. The corresponding colocalization quantization is on the right (n = 15 cells per group, means ± s.d.). **b**, Plasma membrane permeabilization was evaluated with PI uptake assay in stably expressing HA-PD-L1 HeLa cells treated with 250 nM L25K PEI, 100 nM Atz, 25 nM and 100 nM Atz-AUTAB for 1 h. Percentage of cells with PI-positive was quantified (n = 3 biological replicates, means ± s.d.). DNA in **b** was counterstained with Hoechst 33258. Scale bars, 10 µm (**a**) or 100 µm (**b**). Statistical significance was calculated via unpaired two-tailed Student's *t*-test (**a**, **b**).

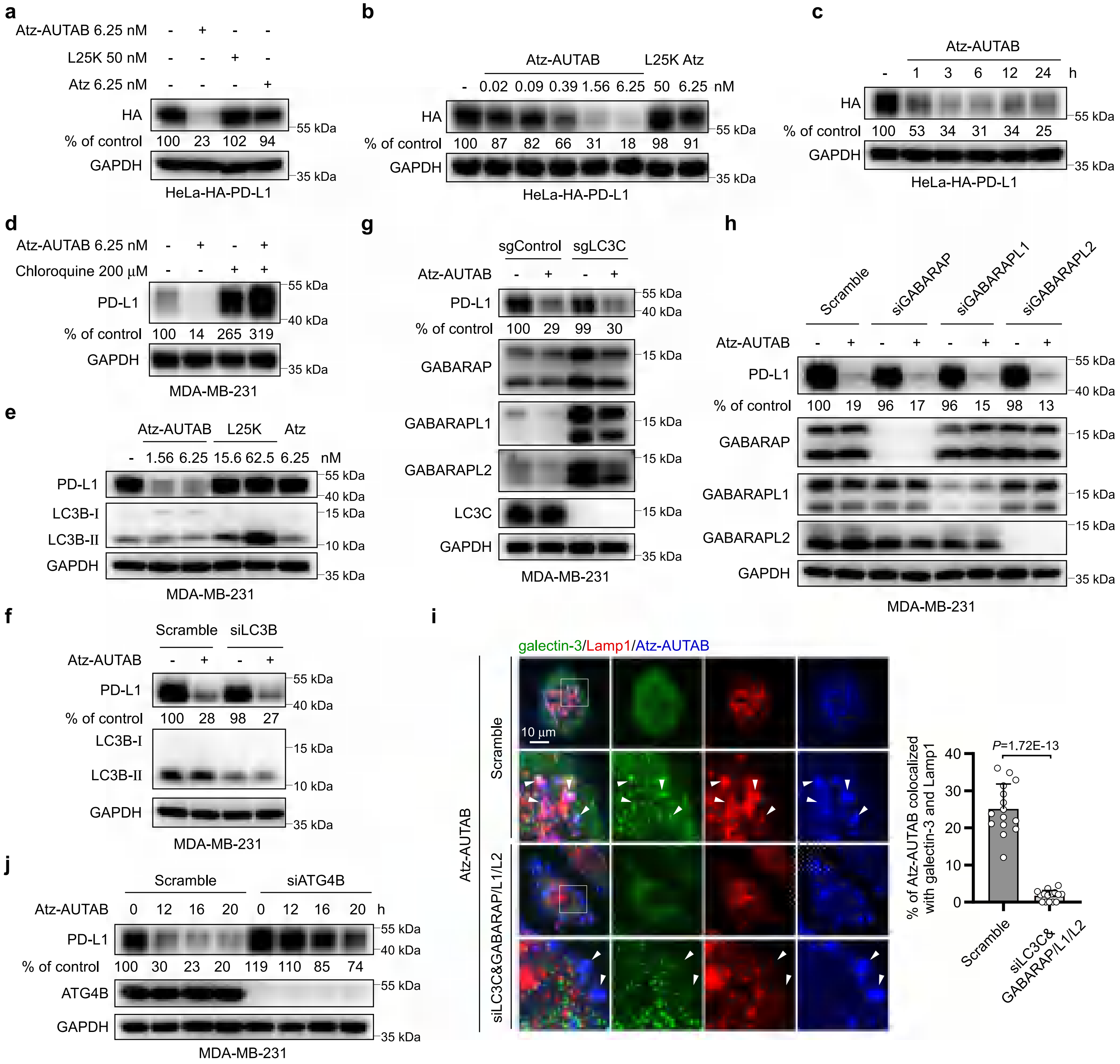

Extended Data Fig. 6 | Mechanical characterization of Atz-AUTAB-mediated PD-L1 degradation. a–c, Degradation of exogenously expressed PD-L1 assessed by western blotting in HA-PD-L1 stably expressing HeLa cells following treatment as in Fig. 3a–c. **d**, Western blot of PD-L1 in MDA-MB-231 cells treated with 6.25 nM Atz-AUTAB for 24 h in the presence or absence of 200 μM chloroquine. **e**, Western blot analysis of PD-L1 and LC3B in MDA-MB-231 cells treated with indicated concentrations of Atz, L25K PEI, and Atz-AUTAB for 12 h and followed by release for 12 h. **f**, MDA-MB-231 cells with or without siRNA mediated knockdown of LC3B were subjected to treatment with 6.25 nM Atz-AUTAB for 12 h. The PD-L1 levels were detected by immunoblotting. **g**, Western blot analysis of GABARAP, GABARAPL1, GABARAPL2 in LC3C knockout MDA-MB-231 cells treated with or without 6.25 nM Atz-AUTAB for 12 h. **h**, Western blot of PD-L1 in MDA-MB-231 cells treated with 6.25 nM Atz-AUTAB for 12 h under siRNA-mediated knockdown of GABARAP, GABARAPL1, and GABARAPL2 respectively. **i**, HA-PD-L1 stable expressing HeLa cells transfected with scramble or LC3C, GABARAP, GABARAPL1, and GABARAPL2 siRNA were incubated with 100 nM Atz-AUTAB for 1 h. Cells were then fixed and co-stained with antibodies against galectin-3, Lamp1 and Atz. The enlarged images of the white box are presented below, with arrowheads indicating the colocalization of galectin-3, Lamp1 and Atz-AUTAB. The quantification is shown on the right (n = 15 cells per group, means ± s.d.). **j**, Western blot of PD-L1 in MDA-MB-231 cells treated with 6.25 nM Atz-AUTAB for the indicated time (0, 12, 16, 20 h) under siRNA-mediated knockdown of ATG4B. Scale bars, 10 μm. Statistical significance was calculated via unpaired two-tailed Student's *t*-test (**i**).

https://doi.org/10.1038/s41589-024-01803-1

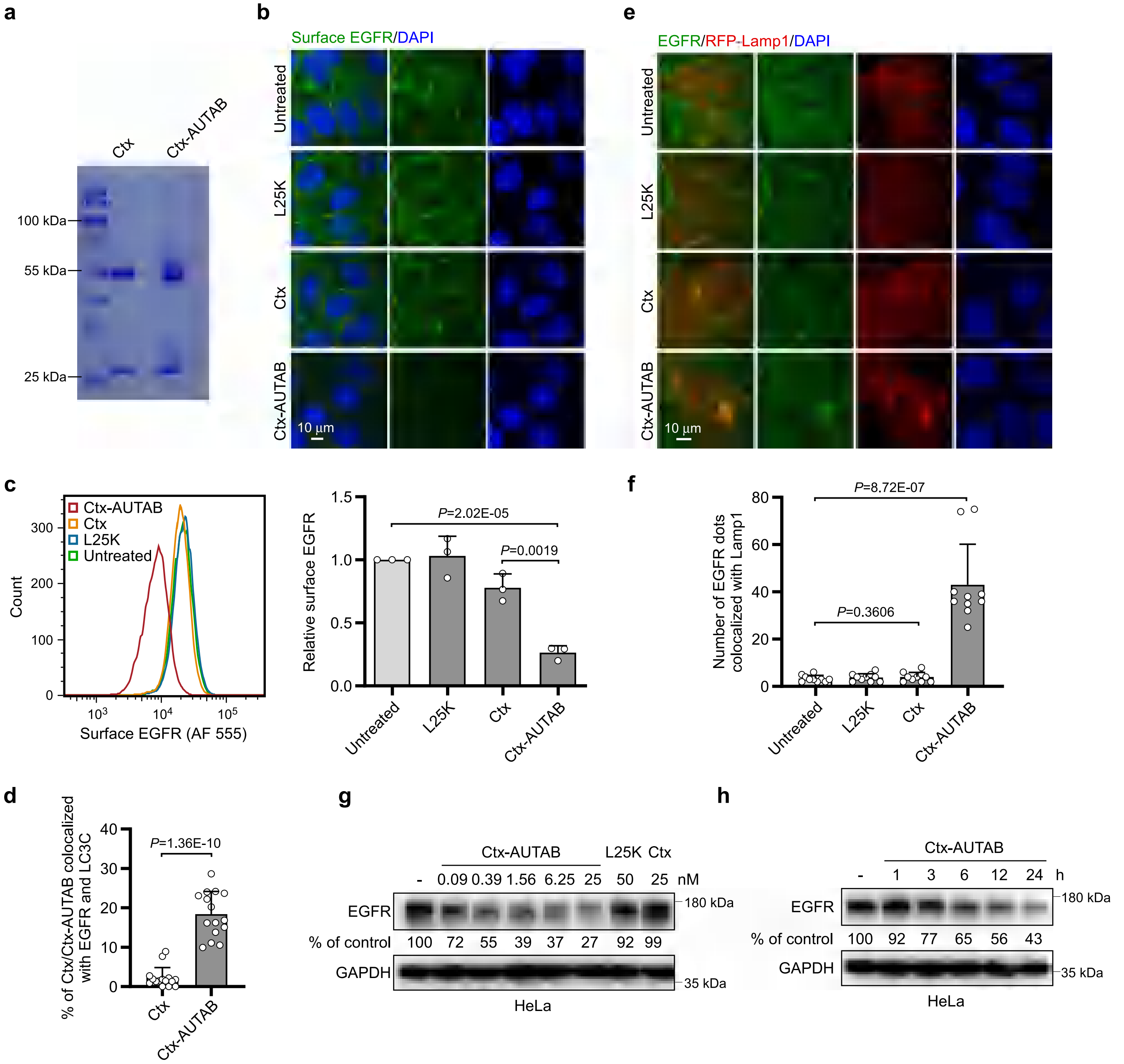

Extended Data Fig. 7 | EGFR degradation driven by Ctx-AUTAB. a, SDS-PAGE analysis of the Ctx-AUTAB with Coomassie blue staining. **b**, Representative surface EGFR immunostaining images of HeLa cells treated with 10 nM L25K PEI, 5 nM Ctx or 5 nM Ctx-AUTAB for 4 h. **c**, Flow cytometry analysis of surface EGFR levels in live HeLa cells upon treatment with 10 nM L25K PEI, 5 nM Ctx or 5 nM Ctx-AUTAB for 4 h. Mean fluorescence intensity of surface EGFR relative to the untreated group was quantified (n = 3 biological replicates, means ± s.d.). **d**, Quantification of triple colocalization between mCherry-LC3C, EGFR and Ctx-AUTAB or Ctx in Fig. 4a (n = 15 cells per group, means ± s.d.). **e**,**f**, Representative confocal images (**e**) and quantification (**f**) showing the colocalization of EGFR and RFP-Lamp1 in HeLa cells following 1 h of treatment with 10 nM L25K PEI, 5 nM Ctx or 5 nM Ctx-AUTAB (n = 10 cells per group, means ± s.d.). **g**, Western blot analysis of EGFR in HeLa cells treated with increasing concentrations of Ctx-AUTAB for 24 h. **h**, Western blot of EGFR in HeLa cells following treatment with 25 nM of Ctx-AUTAB for the indicated time periods. DNA in **b** and **e** was counterstained with DAPI. Scale bars, 10 μm. Statistical significance was calculated via unpaired two-tailed Student's *t*-test (**c**, **d**, **f**).

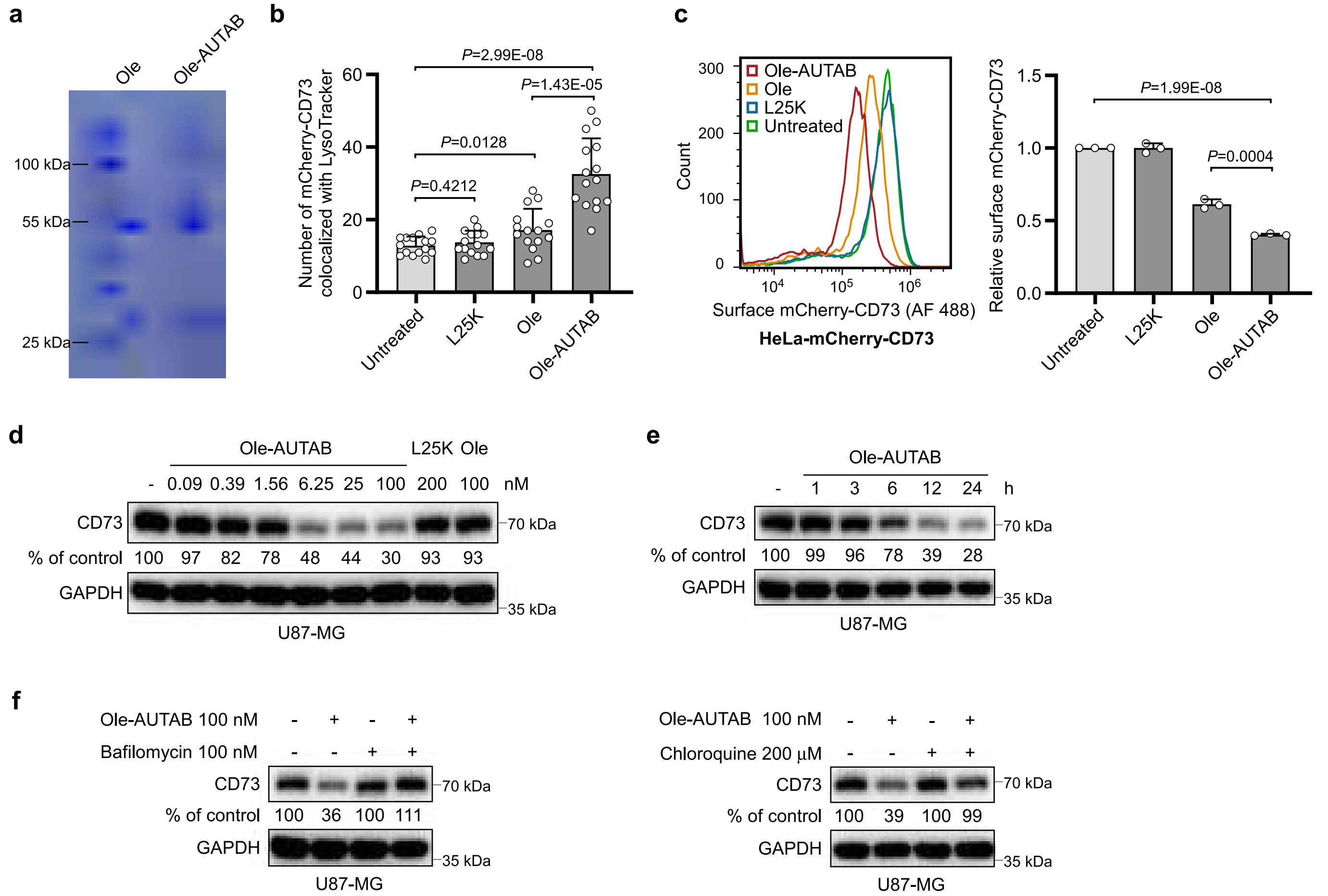

Extended Data Fig. 8 | Ole-AUTAB accelerates CD73 degradation. a, SDS-PAGE analysis of the Ole-AUTAB with Coomassie blue staining. **b**, Quantification of colocalization between mCherry-CD73 and LysoTracker in Fig. 4h (n = 15 cells per group, means ± s.d.). **c**, Live-cell flow cytometry analysis of surface CD73 levels in mCherry-CD73 stably expressing HeLa cells upon treatment with 200 nM L25K PEI, 100 nM Ole or 100 nM Ole-AUTAB for 12 h. Mean fluorescence intensity of surface CD73 relative to the untreated group was quantified (n = 3 biological replicates, means ± s.d.). **d**,**e**, Western blot analysis of CD73 in U87-MG cells upon treatment with increasing concentrations of Ole-AUTAB for 24 h (**d**), or upon treatment with 100 nM of Ole-AUTAB for different times (**e**). **f**, Western blotting to detect the CD73 degradation in Ole-AUTAB treated U87-MG cells in the presence or absence of bafilomycin A1 or chloroquine for 24 h. Statistical significance was calculated via unpaired two-tailed Student's *t*-test (**b**, **c**).

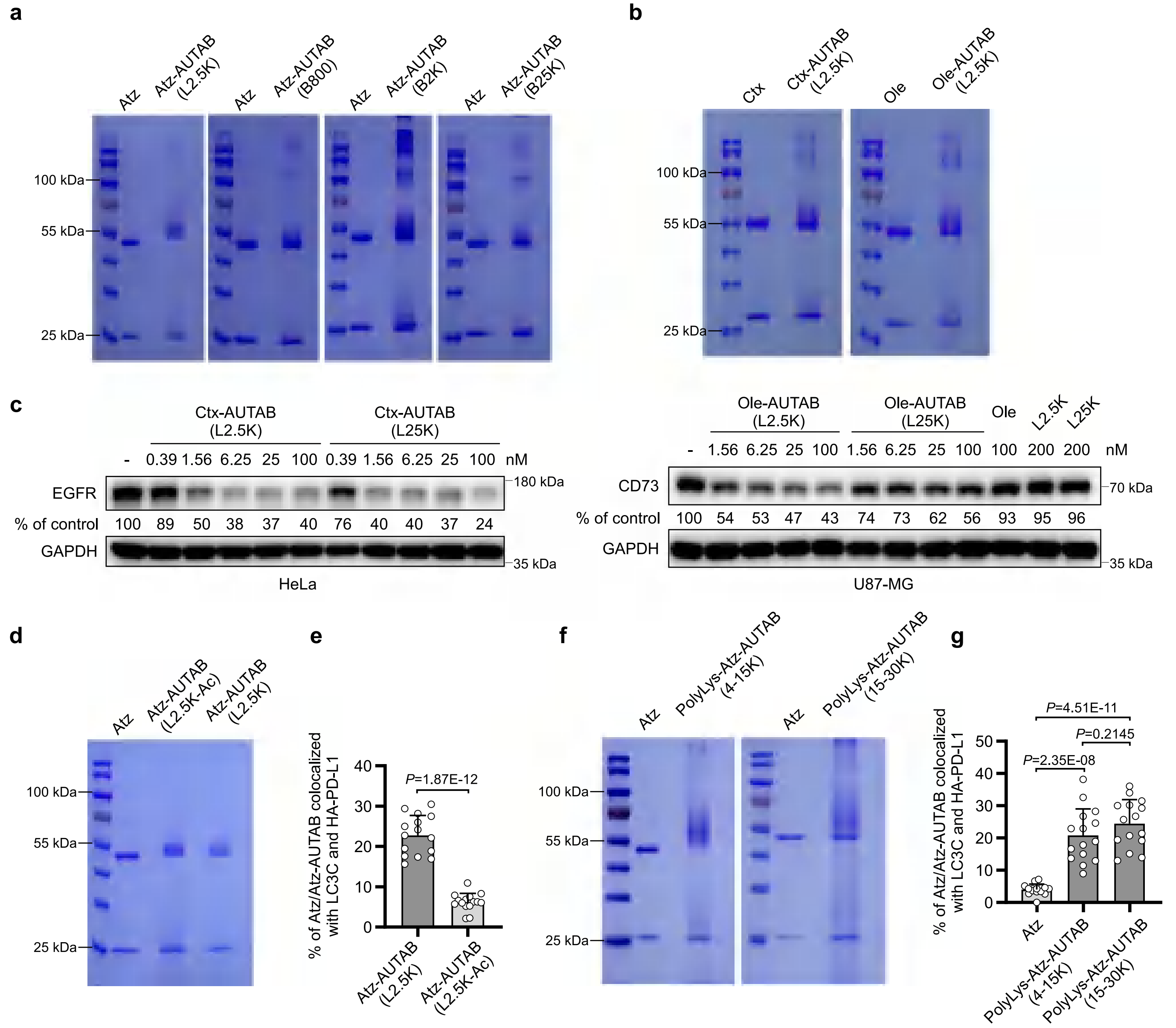

Extended Data Fig. 9 | Gel electrophoresis validation and functional examination of various types of established AUTABs. a,**b**, SDS-PAGE analysis of distinct Atz-AUTABs covalently tagged with various types of PEIs, including L2.5 K PEI, B800 PEI, B2K PEI and B25 K PEI (**a**), and Ctx-AUTAB and Ole-AUTAB that were both conjugated with L2.5K PEI (**b**). **c**, Western blot analysis of EGFR in HeLa cells or CD73 in U87-MG cells that were respectively treated with Ctx-AUTABs or Ole-AUTABs for 24 h at the indicated concentrations. **d**, SDS-PAGE analysis of Atz-AUTABs respectively prepared using acetylated L2.5 K PEI. **e**, Quantification of colocalization between Atz-AUTAB (L2.5 K), mCherry-LC3C and HA-PD-L1 in Fig. 5f (n = 15 cells per group, means ± s.d.). **f**, SDS-PAGE analysis of Atz-AUTABs respectively prepared using poly-L-Lys with varying sizes (4–15 K, and 15–30 K). **g**, Quantification of colocalization between PolyLys-Atz-AUTABs, mCherry-LC3C and HA-PD-L1 in Fig. 5h (n = 15 cells per group, means ± s.d.). Statistical significance was calculated via unpaired two-tailed Student's *t*-test (**e**, **g**).

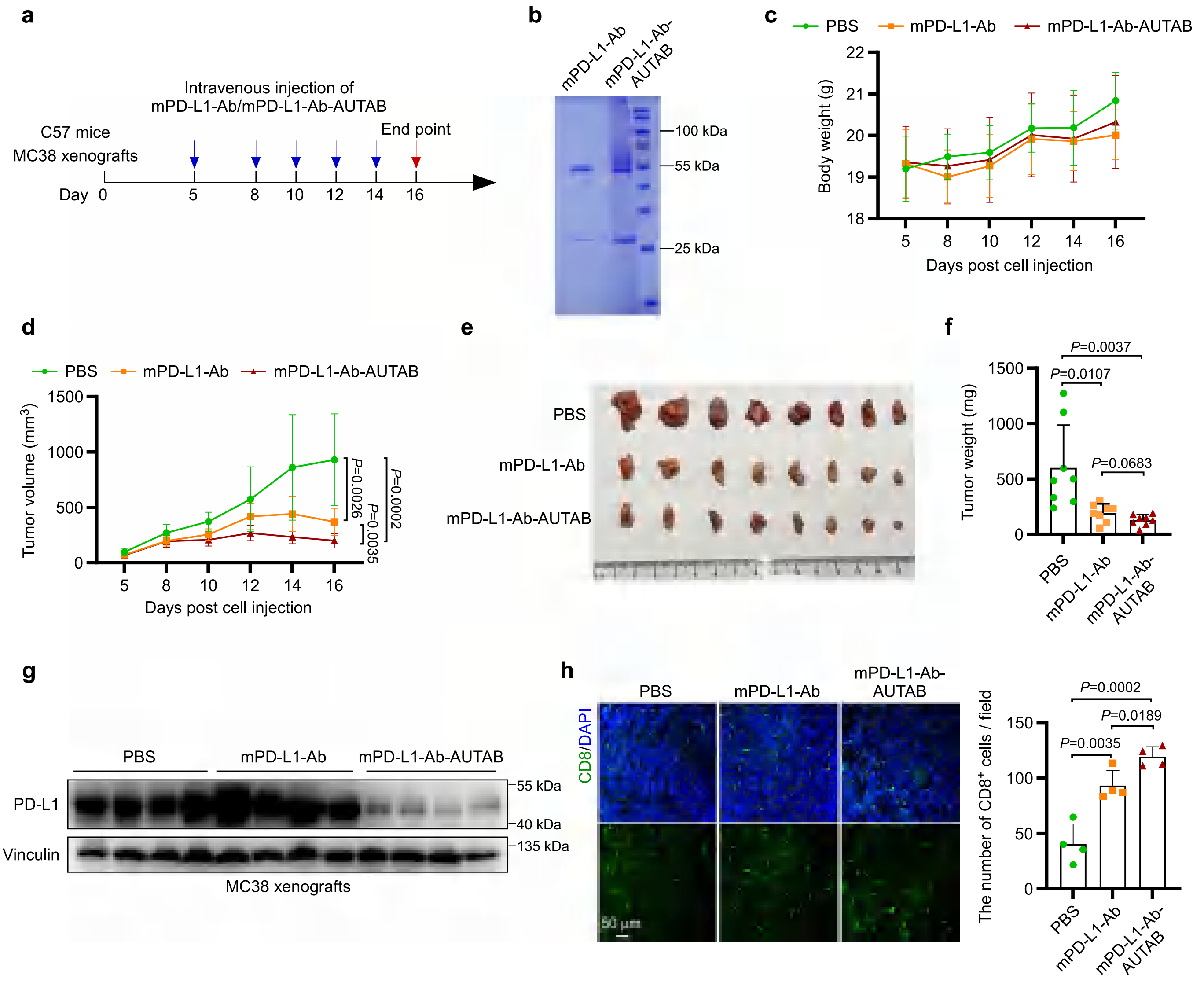

Extended Data Fig. 10 | Therapeutic potential of AUTAB *in vivo*. **a**, Schematic illustration of the general treatment procedure for anti-tumor study. C57BL/6 J mice with MC38 subcutaneous xenografts were administered doses of 5 mg/kg mouse PD-L1 antibody (mPD-L1-Ab) or mPD-L1-Ab-AUTAB by intravenous injection every 2 ~ 3 days for 5 times. **b**, SDS-PAGE analysis of the mPD-L1-Ab-AUTAB with Coomassie blue staining. **c**,**g**, Body weights (**c**) and MC38 tumor volumes (**d**) of mice were monitored during administration with mPD-L1-Ab or mPD-L1-Ab-AUTAB (n = 8 mice per group, means ± s.d.). **e**,**f**, Photographs of excised tumors are shown (**e**) and the weight of tumors was quantified (**f**) at the end of the treatments (n = 8 mice per group, means ± s.d.). **g**, Western blot of PD-L1 in MC38 xenografts in **e** (n = 4 mice per group). **h**, Tumor tissues in **e** were sectioned, stained for CD8, and imaged. The mean number of CD8-positive cells per field was quantified and is shown on the right (n = 4 mice, means ± s.d.). DNA in **h** was counterstained with DAPI. Scale bars, 50 μm. Statistical significance was calculated via unpaired two-tailed Student's *t*-test (**d**, **f**, **h**).